Recent advances in optical fiber high-temperature sensors and encapsulation technique [Invited]

Wenjie Xu (徐文杰)[1], Qiang Bian (卞 强)[2,3,4], Jianqiao Liang (梁建桥)[1], Zhencheng Wang (王振丞)[1], Yang Yu (于 洋)[1*], and Zhou Meng (孟 洲)[4]

[1] Center of Material Science, National University of Defense Technology, Changsha 410073, China

[2] Photonics Laboratory, Munich University of Applied Sciences, Munich 80335, Germany

[3] Institute for Measurement and Sensor Technology, Technical University of Munich, Munich 80333, Germany

[4] College of Meteorology and Oceanography, National University of Defense Technology, Changsha 410073, China

In the aerospace field, for aerospace engines and other high-end manufacturing equipment working in extreme environments, like ultrahigh temperatures, high pressure, and high-speed airflow, *in situ* temperature measurement is of great importance for improving the structure design and achieving the health monitoring and the fault diagnosis of critical parts. Optical fiber sensors have the advantages of small size, easy design, corrosion resistance, anti-electromagnetic interference, and the ability to achieve distributed or quasi-distributed sensing and have broad application prospects for temperature sensing in extreme environments. In this review, first, we introduce the current research status of fiber Bragg grating-type and Fabry–Perot interferometer-type high-temperature sensors. Then we review the optical fiber high-temperature sensor encapsulation techniques, including tubular encapsulation, substrate encapsulation, and metal-embedded encapsulation, and discuss the extreme environmental adaptability of different encapsulation structures. Finally, the critical technological issues that need to be solved for the application of optical fiber sensors in extreme environments are discussed.

Keywords: optical fiber sensors; high-temperature sensing; encapsulation technique; extreme environments.
DOI: 10.3788/COL202321.090007

1. Introduction

With the rapid development of modern aviation and aerospace, there is an increasingly urgent demand for real-time monitoring of multiple physical parameters in extreme environments such as high temperature, high pressure, and high-speed airflow[1–3]. Accurately measuring high-temperature force–thermal distribution and achieving high spatiotemporal resolution visualization monitoring is of great importance for improving the design, health monitoring, and fault diagnosis of major equipment. For example, in the field of aviation engines, the temperature of the post-turbine gas can reach up to 1800°C. Excessive temperatures in the post-turbine gas can reduce the strength of the turbine blade's metal material, increase the tip clearance, cause blade creep and erosion, and in severe cases, lead to structural damage of the engine[4–6]. Therefore, real-time and *in situ* monitoring of the temperature field behind the engine turbine is required. In the field of hypersonic aircraft, the working environment inside the engine combustion chamber involves high temperature, high pressure, and high-speed gas flow. Under extreme flight

conditions, it is easy to exceed the flame stability limit, leading to gradual extinguishing or even complete extinction of the flame inside the engine[7–9]. Therefore, it is necessary to grasp the distribution pattern of high-temperature force–thermal on the combustion chamber wall.

Currently, surface-contact temperature sensors mainly include thermocouples and optical fiber sensors. Technology of thermocouple is mature and widely used, with a temperature measurement range of up to 2300°C[10]. However, thermocouple temperature sensors suffer from common-mode noise interference, poor stability, and susceptibility to oxidation and erosion. Optical fiber sensors have unique advantages, such as high sensitivity, light weight, small size, resistance to electromagnetic interference, corrosion resistance, and distributed sensing[11–13]. However, the stability of conventional silica fibers is relatively poor in ultrahigh-temperature environments, and the doping of germanium or rare-earth ions in fibers can cause thermal diffusion, which reduces the fiber transmission performance, making it unsuitable for stable operation above 1000°C[14]. Sapphire

fibers have been demonstrated to be a better candidate for ultra-high-temperature measurements above 1200°C, due to the advantages of high melting point (∼2050°C), excellent transparency, and chemical corrosion resistance[15–18], but they are susceptible and suffer from multimode problems. Developing new high-temperature sensors with a higher temperature measurement range, multiparameter sensing ability, erosion resistance, and distributed or quasi-distributed sensing capability has good prospects.

Compared with surface-contact sensors, embedded sensors can monitor critical positions inside the structure in real time. Metal-embedded optical fiber sensors have been extensively studied in the past decades due to the advantages of corrosion resistance and erosion resistance[19–22]. Metal-embedded optical fiber sensors can enhance the fatigue resistance of fibers without affecting the integrity and the thermal protection performance of structural components, making them suitable for health monitoring of structures in extreme environments. The embedding method of optical fiber sensors includes ultrasonic additive manufacturing (UAM)[23], laser additive manufacturing, casting[24], electroplating[25], etc.

In this review, we present the current research status of fiber Bragg grating (FBG) and Fabry–Perot interferometer (FPI) optical fiber high-temperature sensors, and summarize the progress of the encapsulation technique for optical fiber high-temperature sensors. We also discuss the extreme environmental adaptability of different encapsulation technique structures, and explore the critical technical issues that need to be addressed for optical fiber sensors used in extreme environments.

2. Optical Fiber High-Temperature Sensor Types and Principles

Optical fiber high-temperature sensors can be divided into FBG-type, FPI-type and blackbody radiation-based type, according to the sensing principle. This paper mainly introduces FBG-based and FPI-based fiber sensors. The sensitive element of the blackbody radiation-based fiber sensor is located in the front of the probe blackbody cavity[26–29]; the optical fiber only is a light-guide medium, and its measurable dynamic range is small and has large error. Therefore, this paper does not expand to the introduction of blackbody radiation-based fiber sensors.

2.1. FBG-type high-temperature sensors

FBG is a wavelength-specific reflector that is formed by inducing a periodic modulation of the refractive index in the core of an optical fiber with ultraviolet (UV) light or femtosecond lasers. The Bragg wavelength λ_B is defined by the effective refractive index n_{eff} and the grating period Λ with the following relationship:

$$\lambda_B = 2n_{\text{eff}}\Lambda. \tag{1}$$

By monitoring the Bragg wavelength change $\Delta\lambda_B$ as a function of temperature, the temperature sensitivity of FBG K_T can obtained[30],

$$K_T = \frac{\mathrm{d}\lambda}{\mathrm{d}T} = \lambda_B(\alpha + \zeta), \tag{2}$$

where α is the coefficient of thermal expansion (CTE) and ζ is the thermo-optic coefficient.

It has been found that there is a nonlinear relationship between the Bragg wavelength change and temperature in a wide temperature range[31]. The wider the temperature range is, the more obvious the nonlinearity appears. A polynomial function of temperature T can also be used to show this relationship,

$$\Delta\lambda_B(T) = \sum_{i=0}^{n} a_i T^i, \tag{3}$$

where a_i are polynomial coefficients.

It should be noted that FBG is inherently sensitive both to temperature and strain, as both n_{eff} and Λ vary with those two parameters, leading to the Bragg wavelength change. Therefore, solving the cross-sensitivity issue of temperature and strain is of great significance.

Since Hill et al.[32] inscribed the first FBG in 1978, FBGs have been widely applied for temperature sensing in the past several decades. For conventional FBGs written by UV light, which are called Type-I FBGs, the refractive index will decay or even be erased when the temperature exceeds 300°C[33], making it difficult to meet the requirement of high-temperature sensing. Several different methods, such as CO_2 laser writing[34], high-temperature annealing[35], and femtosecond laser writing[36], have been proposed to improve the upper temperature resistance limit of FBGs, making it possible to monitor temperature gradients in nuclear reactors and temperature distributions in gas turbines under high-temperature environments[31,37,38].

Huang et al.[34] fabricated a long-period fiber grating (LPFG) high-temperature strain sensor using CO_2 laser induction and encapsulated it to achieve temperature sensing in the range of 700°C with large strain measurement in the range of 15,000 µε with a strain resolution of 0.5 µε.

Regenerated fiber Bragg grating (RFBGs) are produced by subjecting pretreated seed gratings (Type-I FBGs) to a thermal annealing process at high temperatures, typically in the hundreds of degrees Celsius. During this process, the reflectivities of the seed gratings gradually decay to almost zero and then regrow to a relatively low level, which is the origin of the term "regenerated." To date, despite extensive research, there is currently no comprehensive explanation for the mechanisms behind the regeneration effect in RFBGs. However, two alternative theories have been proposed: the chemical composition theory and the crystallization theory[39]. The chemical composition theory was proposed by Fokine et al.[40] in 1997, where RFBGs are regarded as oxygen–chemical composition gratings that are formed at high temperatures. In the fiber core, the concentration of oxygen is periodically modulated in the illuminated and nonilluminated areas. In 2008, Canning et al.[35] proposed crystallization theory, and they believe that it is the high temperature that reduces tensile core–cladding interface stresses and even inverts those stresses in the illuminated areas

into compressive stresses, which causes crystallization and refractive index modulation in those areas. Both of these theories have been supported by various experimental observations, but neither one of them can fully explain all of the phenomena related to regeneration.

In 2015, Yang et al.[41] fabricated two cascaded Type-I FBGs with center wavelengths of 1304 nm and 1547 nm, respectively, and obtained RFBGs by annealing. Simultaneous high temperature and strain measurements were achieved within the temperature and strain ranges of 900°C and 1000 μɛ. In 2020, Gunawardena et al.[42] reported for the first time a resurgent regenerated fiber Bragg grating (R²FBG). An FBG was inscribed in a six-hole microstructured optical fiber (SHMOF), followed by high-temperature annealing to generate RFBG. The generated RFBG was rapidly heated, resulting in its disappearance at 1363°C and the regeneration of a new grating at 1405°C. Subsequently, the R²FBG was formed by rapid cooling to room temperature. Figure 1(a) illustrates the response of the peak power and wavelength shift of the RFBGs in SHMOF. Figure 1(b) shows the reflection spectra of the RFBG and the R²FBG at various temperatures throughout the heating process. It was demonstrated that this R²FBGs could be applied for ultra-high-temperature measurements exceeding 1400°C.

Over the past 10 years, the suitability of RFBGs as temperature sensors for high-temperature applications has been investigated.

In 2015, Rinaudo et al.[43] demonstrated the feasibility of RFBG application for temperature monitoring in the case of building fires. The RFBG sensor was mounted on concrete and tested for 1 h according to the ISO-834 fire curve. The sensor was subjected to direct flame and high-speed temperature rise of 200°C/min, and the highest gas temperature measured was about 970°C, demonstrating the feasibility of the RFBG sensor for real fire monitoring. The research results are instructive for fire protection engineering research and applications.

In 2018, Dutz et al.[44] reported the application of RFBG arrays for high-temperature distribution measurements in chemical reaction vessels and gas turbine exhausts. 24-point RFBG and three-point RFBG arrays were used to measure the temperature change profiles of chemical catalytic reaction processes and the temperature gradients in gas turbine exhausts,

respectively, and their maximum temperatures in both cases did not exceed 550°C. This study demonstrated that RFBG array-type temperature sensors can be used for high-temperature measurements in harsh industrial environments.

In 2018, Laffont et al.[38] applied the RFBG array high-temperature sensor encapsulated in metallic capillaries to the temperature measurement of liquid sodium in a nuclear reactor, as shown in Fig. 2. The sensor measured the temperature gradient of liquid sodium during heating from 47°C to 500°C, with a response time of 144 ms. The research results demonstrate the feasibility of RFBG application in high-temperature and high-radiation nuclear reactors, and show the capability of RFBG for structural health monitoring in nuclear power plants and nuclear reactors.

In recent years, with the development of laser processing technology, ultrafast lasers, typically femtosecond lasers, have been widely applied for the inscription of FBGs in silica-based fibers[45]. The high intensity of femtosecond laser pulses can cause physical damage to the fiber core, resulting in permanent refractive index modulation. The grating inscribed by the high-energy laser is called a Type-II FBG, which shows a temperature stability similar to that of RFBGs[39].

In 2004, Martinez et al.[46] first used the femtosecond laser point-by-point inscription method to inscribe first- to third-order FBGs in single-mode fibers (SMFs) and dispersion-shifted
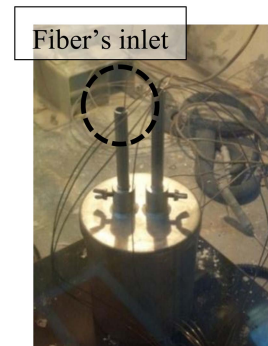

Fig. 2. Experimental photograph of liquid sodium temperature measurement using RFBG sensor[38].
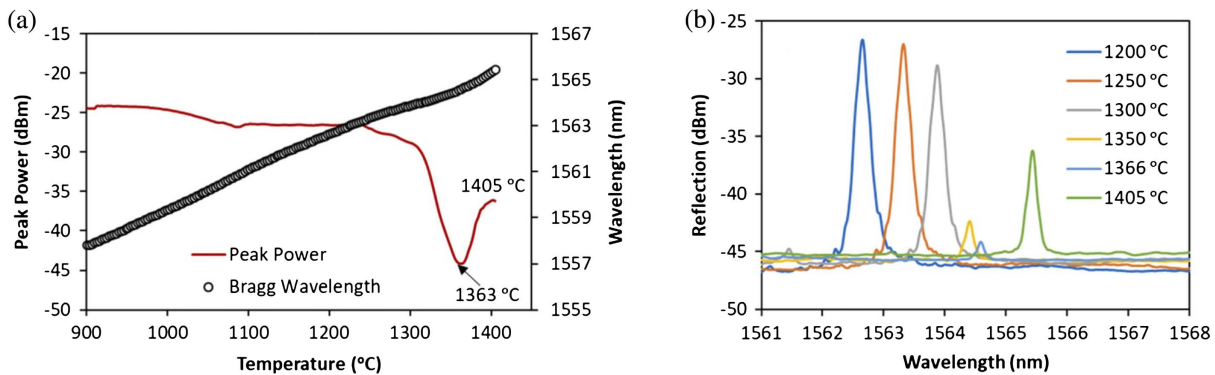

Fig. 1. (a) Peak power, wavelength shift and (b) reflection spectra of an RFBG/R²FBG with increasing temperature[42].

fibers (DSFs), respectively. In 2006, Grobnic et al.[47] showed that Type-II FBGs exhibit remarkable thermal stability up to 1000°C for 150 h. A reflectivity decay and a permanent drift of Bragg wavelength were observed at temperatures exceeding 1050°C. In 2011, Li et al.[48] annealed Type-II FBGs at 1000°C, and after the air quenching and the pre-stress treatment, those FBGs were able to operate stably for 26 h at 1200°C. In 2019, Warren-Smith et al.[49] studied the high-temperature stability of Type-II FBGs using femtosecond laser etching on silica suspended-core fibers, where the sensor was stable at 700°C for approximately 300 h, as well as at up to 1100°C for 48 h. The thermally annealed sensor showed higher stability at temperatures less than 1050°C, with a sensor temperature drift of less than 0.5°C/day at 1050°C. The effect of long-term annealing on the high-temperature stability of the sensor was further investigated by Grobnic et al.[50] in 2021, who annealed Type-II FBGs at 1000°C for several hundred hours, and the temperature drift of the annealed sensors was reduced to 0.03°C/h at 900°C.

Studies have shown that Type-II FBGs have excellent high-temperature stability, and they have been used for temperature measurements in the real industrial scenarios.

In 2013, Xia et al.[1] monitored the circumferential and radial temperature distribution at the outlet of a gas turbine engine using a Type-II FBG array. After calibrating the sensor for the temperature range of 0°C to 650°C, the sensor was installed at the gas turbine engine exhaust, and its long-term thermal stability was monitored. The results showed that the sensor exhibited comparable performance to thermocouples with approximately 9°C fluctuations over 100 min.

In 2018, Walker et al.[51] implemented the monitoring of temperature gradients over the combustion chamber flame tube using a Type-II FBG array encapsulated in a chromium–nickel (Ni) alloy tube, as shown in Fig. 3. Combustion tests showed that the sensor exhibited good thermal repeatability, withstood multiple thermal cycles, and sustained temperatures up to 900°C. The distributed Type-II FBG sensor can significantly reduce wiring compared to thermocouple temperature sensors, showing great advantages in aerospace applications such as gas turbine monitoring.

In 2018, Zaghloul et al.[52] inserted the Type-II FBGs into a Massachusetts Institute of Technology (MIT) research nuclear
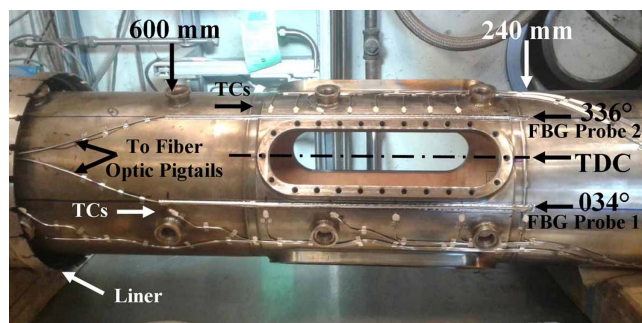

Fig. 3. Photograph of the combustion chamber flame tube arrangement of Type-II FBG array temperature probe[51].

reactor (6-MW, at a temperature > 600°C) for sensing temperatures. The results show that the FBG sensors can survive extreme environments of the nuclear reactor cores under intense gamma and neutron irradiation at high temperatures.

However, it should be noted that silica-based optical fibers are limited by their material softening point, and it would be challenging for those sensors to maintain long-term stability in high-temperature environments above 1000°C[14]. Even with processes such as quenching and annealing, the maximum measurable temperature can barely be achieved at 1400°C[42].

Compared with silica-based optical fibers, sapphire fibers exhibit some superior properties such as high melting point (2053°C), high hardness, and chemical corrosion resistance[53]. In recent years, they have attracted extensive attention in the field of high-temperature sensing. The multiphoton absorption also applies to other materials, so Type-II FBGs can be inscribed in sapphire fibers as well, which are called sapphire fiber Bragg gratings (SFBGs). There are typically three different methods for inscribing SFBGs: the phase mask method[16], the point-by-point method[54], and the line-by-line scanning method[55].

In 2004, Grobnic et al.[16] for the first time inscribed an SFBG using a 800 nm femtosecond laser and the phase mask method. The fifth-order grating with a pitch period of 2.14 μm was on a sapphire fiber with a diameter of 150 μm; its microscope image is shown in Fig. 4(a). Figure 4(b) shows the reflectance spectrum of the SFBG at room temperature. It can be seen that, due to the multimode characteristics of sapphire fibers, the reflected lights contain various modes, leading to a broad linewidth of the reflection spectrum. To solve this problem, Grobnic et al.[56] in 2006 used the mode filtering effect to fuse a tapered SMF to a sapphire fiber to obtain an SFBG with a 3 dB bandwidth of 0.33 nm, enabling ultrahigh temperature measurements at 1500°C.

In 2009, Busch et al.[57] further tested the temperature response of the SFBG in the range of 20°C–1745°C. When the temperature exceeded 1400°C, the signal-to-noise ratio (SNR) of the spectrum decreased significantly due to the increased blackbody radiation, and the reflection intensity of the SFBG decreased significantly, which indicated that the SFBG could not operate at high temperatures above 1400°C for a long time. In 2015, Habisreuther et al.[58] measured the temperature distribution in a high-temperature tube furnace using an SFBG prepared by a femtosecond laser, as shown in Fig. 5. By moving the high-temperature furnace at a speed of 5 cm/min, the sensor measured the temperature distribution in the high-temperature tube furnace at 1500°C with a measurement error of less than 2°C. The authors also raised the temperature to 1900°C by filling the furnace with argon gas, and the SFBG still survived. Their research results show that SFBG has the potential for 1900°C temperature sensing.

In 2022, He et al.[59] encapsulated SFBGs with a sapphire tube and inert gas, solving the high transmission loss issue caused by high-temperature oxidation. The schematic diagram of the encapsulation technique structure is shown in Fig. 6. The results demonstrated that the encapsulated sensor could operate stably
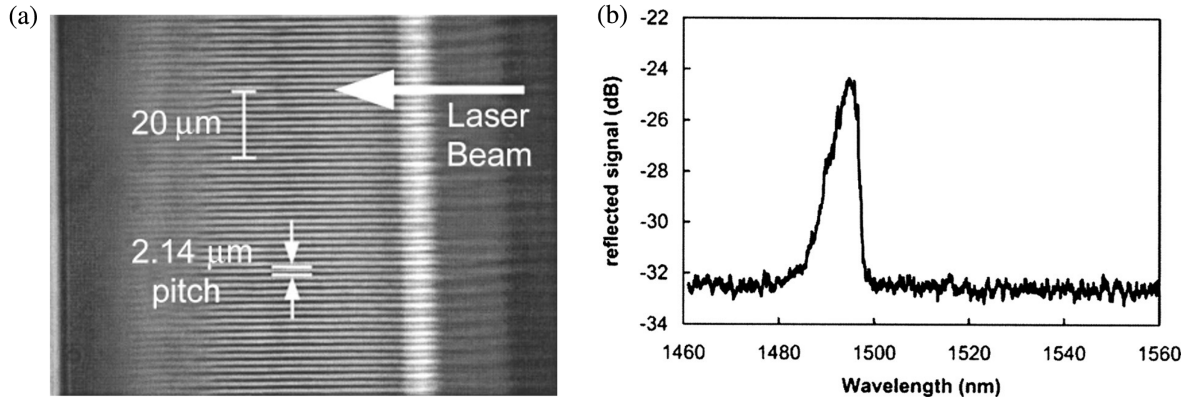
Fig. 4. (a) Photograph of SFBG structure; (b) reflection spectrum of SFBG at room temperature[16].
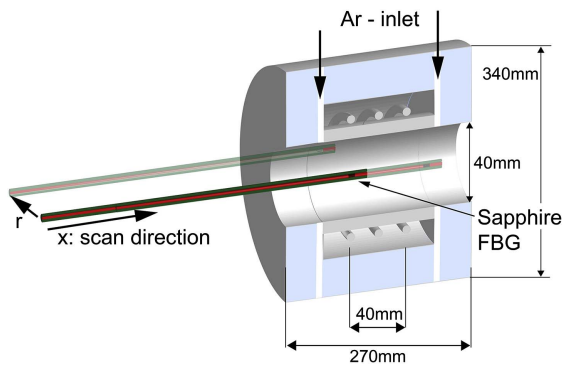

Fig. 5. Schematic diagram of the temperature distribution inside an inductively heated furnace using SFBG scanning[58].
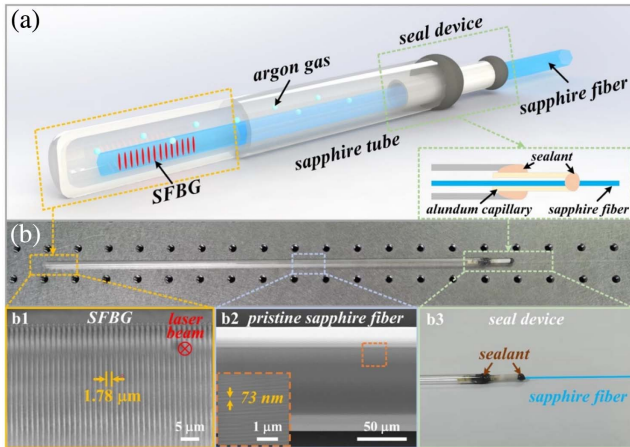

Fig. 6. (a) Schematic diagram of SFBG sensor; (b) physical image of the sensor[59].

for 20 h at 1600°C, with a maximum operating temperature of 1800°C.

SFBGs have demonstrated excellent performance in the field of ultrahigh-temperature sensing and have the potential to meet the high-temperature sensing requirements of complex force-heat environments such as aviation engines and hypersonic aircraft. However, there are still several issues that need to be solved in the practical application of SFBG, such as the connection difficulty between sapphire and silica fibers, the multimode behavior of reflection spectra, and the cross talk in multiparameter sensing of SFBGs.

The high-temperature sensing performance of different material fibers and different types of FBGs is summarized in Table 1. The term "Type" in Table 1 and in the rest of this paper refers to the underlying photosensitivity mechanism by which grating fringes are produced in the optical fiber[60].

2.2. FPI-type high-temperature sensors

The sensitive element of the fiber FPI temperature sensor is the F–P cavity. When the ambient temperature changes, the refractive index of the fiber and the length of the F–P cavity change accordingly, due to the thermo-optical effect and the thermal expansion, which leads to a change in the optical path difference and causes a change in the phase, in turn leading to a wavelength drift in the interferometric spectrum. The sensing of external temperature is achieved by demodulating the interferometric spectrum. The wavelength of the interferometric trough of FPI can be expressed as

$$\lambda = \frac{2nL}{m}, \tag{4}$$

Table 1. Performance Comparison of FBG High-Temperature Sensors.

Fiber Material	FBG Type	Max	Stable
Silica	Type-I FBGs	450°C[61]	~320°C
	RFBG	1452°C[42]	1350°C
	Type-II FBGs	1000°C[50]	1000°C
Sapphire	SFBG	1900°C[58]	1500°C

where n is the refractive index of the medium, m is the number of interference order, and L is the cavity length.

The temperature sensitivity is denoted as

$$K_T = \frac{\Delta\lambda}{\Delta T} = \left(\frac{1}{L}\frac{\Delta L}{\Delta T} + \frac{1}{n}\frac{\Delta n}{\Delta T}\right)\lambda = (\alpha + \zeta)\lambda, \qquad (5)$$

where $\Delta\lambda$ is the change in wavelength, Δn is the change in refractive index, ΔT is the change in temperature, α is the CTE, and ζ is the thermo-optic coefficient.

The FPI temperature sensors are susceptible to external disturbances. For example, the external strain acting on the F–P cavity causes compression or stretching of the cavity length L, leading to a wavelength drift in the interference spectrum. As with FBG sensors, the cross-sensitivity of temperature and strain for FPI sensors is also an important issue needing attention.

FPI can be divided into the intrinsic Fabry–Perot interferometer (IFPI) and the extrinsic Fabry–Perot interferometer (EFPI), according to the structure of the sensitive element. Table 2 summarizes the performance parameters of IFPI and EFPI high-temperature sensors in recent years. Due to the thermo-optical effect, IFPI is more sensitive to temperature than strain or pressure[67,79,80]. From Table 2, it can be seen that IFPI is often used

for temperature sensing and less often for strain sensing. For the fabrication of fiber FPI high-temperature sensors, high-temperature resistant materials such as silica, sapphire, and silicon carbide are usually used. Currently, scholars have used high-temperature-resistant materials combined with femtosecond laser micro- and nanoprocessing[81], micro-electro-mechanical systems (MEMS) processing[82], and CO_2 laser welding[83] to develop high-temperature fiber FPI sensors.

Optical fiber FPI-type sensors were first developed in 1982 by Yoshino et al.[84] and applied for sensing temperature, mechanical vibration, acoustic wave, AC voltage and AC and DC magnetic fields. In 1991, Lee et al.[85] fabricated an IFPI temperature sensor by fusing a section of TiO_2-coated fiber to an SMF to achieve 108°C temperature measurement. In 2008, Choi et al.[86] made a compact FPI sensor by splicing a section of hollow-core fiber (HCF) and a section of SMF to PCF, and achieved high temperature sensing from 50°C to 1000°C. Benefiting from the development of femtosecond laser micromachining technology, in 2008, Wei et al.[87] used a femtosecond laser to micro-machine a groove in an SMF to form an EFPI temperature sensor, as shown in Fig. 7, and the cavity length of the sensor was measured to be 30 µm by scanning electron microscopy (SEM), with an ablation depth of ~72 µm. Its interference

Table 2. Performance Comparison of IFPI and EFPI.

| FPI Type	Characteristic	Operating Temperature	Temperature Sensitivity	Operating Strain	Year
IFPI	Dispersion compensation fiber (DCF)	25°C–600°C	68.6 pm/°C		2009[62]
	Microstructured fiber (MF)	24°C–1000°C	17.7 pm/°C		2013[63]
	Double-core photonic crystal fiber (DC-PCF)	30°C–900°C	13.9 pm/°C		2014[64]
	PCF	17°C–1200°C	10 pm/°C		2015[65]
	Microfiber (MF)	25°C–1000°C	13.6 pm/°C		2018[66]
	No-core fiber (NCF)	100°C–1100°C	16.36 pm/°C (400°C)	0–2000 µε	2019[67]
	Polarization-maintaining PCF	100°C–1000°C	15.34 pm/°C		2020[68]
	PCF	25°C–1000°C	16.12 nm/°C		2021[69]
	Polarization-maintaining PCF	50°C–900°C	17.52 pm/°C (400°C)		2021[70]
EFPI		100°C–700°C	0.98 pm/°C	0–800 µε	2012[71]
		20°C–800°C	0.59 pm/°C	0–3700 µε	2014[72]
		23°C–600°C	12.3 pm/°C	0–2104 µε	2016[73]
		20°C–1000°C	15.41 pm/°C	0–1 000 µε	2019[74]
		100°C–800°C	10.74 pm/°C	0–900 µε	2020[75]
		26°C–1000°C	6.98 pm/°C (800°C)	0–350 µε	2022[76]
		26°C–700°C	12.715 pm/°C		2022[77]
		24°C–900°C	12.8 pm/°C	0–210 µε	2023[78]
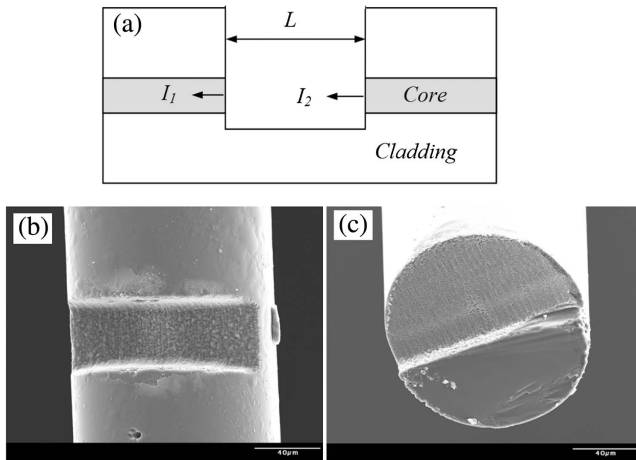
Fig. 7. (a) Schematic diagram of the FPI structure; (b) SEM top view; (c) SEM cross-sectional view of the FPI structure[87].

spectrum had an extinction ratio greater than 14 dB, and tests showed that the sensor could achieve temperature sensing up to 1100°C, with a sensitivity of 0.074 pm/°C.

In 2014, Kaur et al.[72] micromachined an FPI microcavity on the end face of an SMF using femtosecond laser micromachining technology to achieve temperature sensing at 800°C, and performed a strain measurement at room temperature up to 3700 µε. In 2019, Lei et al.[88] reported an IFPI high-temperature sensor based on hollow-core photonic crystal fiber (HC-PCF), the structure of which is shown in Fig. 8. It was formed by splicing a section of HC-PCF in between an SMF and a piece of pure silica. The results showed that the sensor could achieve high-temperature sensing up to 1200°C with excellent linearity and had a temperature sensitivity of 15.68 pm/°C.

The highest temperature measurement limit of silica-based optical fiber FPI temperature sensor is 1200°C[88,89]. In order to further improve the temperature measurement limit, many scholars have proposed the FPI temperature sensor based on sapphire fiber[90–92].

In 1992, Wang et al.[93] fabricated an IFPI sensor by fusing a section of sapphire fiber to an SMF and applied the sapphire FPI sensor to high-temperature sensing for the first time, achieving a resolution of 0.2°C at 310°C–976°C. To further improve the upper limit of temperature measurement, in 2006, their team[94] made an EFPI high-temperature sensor by bonding a 45° polished sapphire fiber to the surface of a sapphire wafer, which achieved temperature sensing up to 1170°C, with a resolution of 0.4°C. In 2019, Yu et al.[95] proposed an EFPI high-temperature sensor based on sapphire fiber and sapphire wafer, as shown in Fig. 9. The sensor used a sapphire sleeve to fix two polished sapphire optical fibers with a sapphire wafer to form an F–P cavity structure, and the other end of the sapphire optical fiber was fused to a multimode fiber to achieve long-distance transmission. The sensor used two sapphire fibers to isolate the input and output so as to achieve the separation of background light and interference signal, which significantly improves the fringe contrast and SNR of the interference signal. Test results showed that the sensor could achieve temperature sensing up to 1080°C, and the temperature resolution was better than 0.25°C.
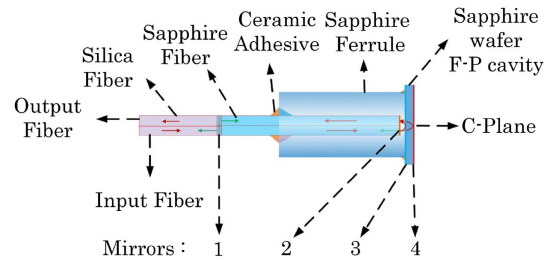

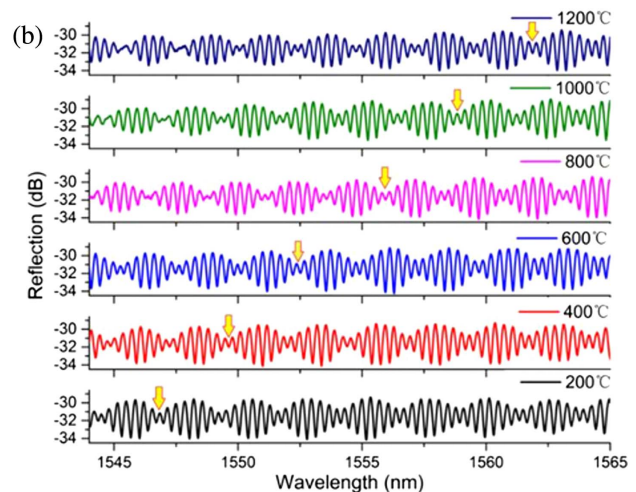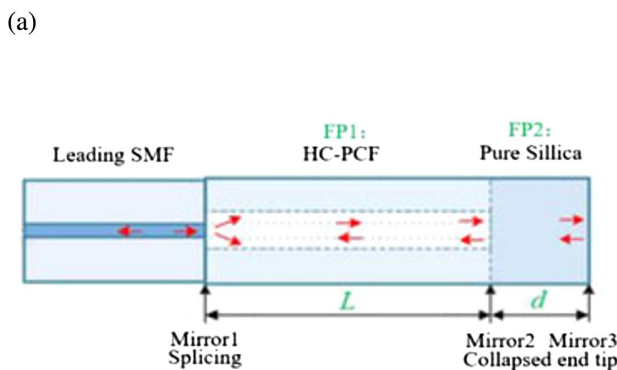**Fig. 9.** Schematic diagram of sensor probe structure[95].

Fig. 8. Optical fiber sensor based on HC-PCF. (a) Schematic diagram of the sensor structure; (b) reflection spectra under different temperatures varying from 200°C to 1200°C[88].

In 2020, Yang *et al.*[96] fabricated an all-sapphire microfiber FPI high-temperature sensor by machining a cylindrical micro-gas cavity on the end face of a sapphire fiber using a femtosecond laser and welding a sapphire wafer to the end of the sapphire fiber using the CO_2 laser fusion technique. The results showed that the sensor was capable of temperature sensing up to 1455°C, with an average temperature resolution of 0.68°C.

The high-temperature sensing performance of different material fibers and different structures of FPIs is summarized in Table 3.

3. Fiber High-temperature Sensor Encapsulation Technique

At present, optical fiber high-temperature sensors are widely used in high-temperature sensing. Those real harsh environments, however, involve not only high temperature but also other factors, such as high pressure, high-speed air flow erosion, and corrosion. Therefore, it is necessary to encapsulate the sensors to enhance their adaptability and robustness. The encapsulation technique for fiber high-temperature sensors in this section can be classified into three kinds: tubular encapsulation[97–102], substrate encapsulation[103–106], and metal-embedded encapsulation[107–112].

3.1. Tubular encapsulation

Tubular encapsulation is a cost-effective approach to improving the reliability and fatigue resistance of high-temperature sensors. In this technology, high-temperature-resistant tubing is typically used to encapsulate the sensor with single or multilayer protection. The resulting encapsulated sensor has good stability, erosion and corrosion resistance, and high mechanical strength, and is suitable for high-temperature measurements in various engineering applications.

Since the mechanical strength of RFBG decreases under high-temperature annealing and is prone to fracture after annealing, RFBG needs to be encapsulated and protected to meet practical applications. In order to improve the fatigue resistance of RFBG, in 2011, Barrera *et al.*[113] used an alumina ceramic tube and a Ni alloy shell to encapsulate an RFBG sensor, as shown in Fig. 10. First, the seed grating was encapsulated in a composite structure with an inner ceramic tube and an outer Ni alloy shell using high-temperature ceramic glue, and then the encapsulated sensor was annealed at 1000°C to generate the RFBG. The tests on the encapsulated sensor showed that the encapsulated sensor could achieve temperature sensing up to 1100°C without exhibiting any hysteresis, and its time response was about 9 s, consistent with the performance of the corresponding thermocouples.

To prevent the formation of microcracks and devitrification on the fiber surface at high temperatures, in 2014, Mamidi *et al.*[114] used five different tubular encapsulation materials: silicon carbide, borosilicate glass, stainless steel, copper (Cu), and aluminum nitride for Type-I FBGs, respectively. The effect of different encapsulation materials on the temperature response

Fig. 10. Physical image of RFBG sensor encapsulated in alumina ceramic tube and Ni alloy shell[113].

Table 3. Performance Comparison of FPI High-Temperature Sensors.

Fiber Material	Structure	Operating Temperature	Temperature Sensitivity Sensing Performance	Year
Silica	SMF coated with TiO_2 film	26°C–108°C	1.53 rad/°C	1991[85]
	PCF-HCF-SMF	50°C–1000°C		2008[86]
	Groove micromachined by femtosecond laser	0°C–1100°C	0.074 pm/°C	2008[87]
	Microcavity fabricated by femtosecond laser	50°C–800°C	0.59 pm/°C	2014[72]
	SMF-HC-PCF	200°C–1200°C	15.68 pm/°C	2019[88]
Sapphire	SMF-SF-PCF	310°C–976°C	1.26 rad°C^{-1} mm^{-1}	1992[93]
	45° SF-sapphire wafer	24°C–1170°C	1.524–2.322 nm/°C	2006[94]
	SF-sapphire wafer	100°C–1080°C	4.786 nm/°C	2019[95]
	SF-air cavity-sapphire wafer	0°C–1455°C	1.32–2.45 nm/°C	2020[96]

of the sensor was investigated in the temperature range of 20°C–500°C. The experiments showed that the response of the Cu-encapsulated fiber grating exhibited a slight nonlinearity, and the aluminum nitride encapsulation showed better linearity and faster response compared to the other three materials. In 2015, Mamidi et al.[100] encapsulated a femtosecond laser-inscribed FBG in stainless steel and ceramic tubes. The Type-II FBG was first encapsulated in an aluminum nitride (ceramic) capillary tube to achieve strain isolation and then protected using a stainless-steel tube. The sensor probe was further inserted in a steel rod by making use of a brass holder and was sealed with a high-temperature adhesive. The sensor was used as a temperature probe with a measuring range of up to 650°C and a resolution of 1°C.

In 2018 Wilson et al.[115] found that sapphire fibers generated some form of aluminum hydroxide on the fiber surface due to high-temperature oxidation in high-temperature environments at 1400°C and above, resulting in a significant increase in the transmission loss of sapphire fibers, which seriously affects their optical transmission performance. To address this problem, their team used an inert gas to isolate the sapphire fiber from the outside air and found that any surface layers generated by high-temperature oxidation of the sapphire fiber were completely eliminated at 1400°C. Their research results showed that the inert gas could inhibit the high-temperature oxidation of sapphire fiber. In 2019, Yang et al.[116] fabricated an SFBG array by the point-by-point method, which was then encapsulated using a sapphire tube, as shown in Fig. 11. The encapsulated sensor was annealed at 1000°C for 110 h, and the calibrated sensor was used to measure the temperature field of commercial coal-fired and gas-fired boilers, achieving long-term stable testing up to 1200°C. In 2022, He et al.[59] further raised the temperature limit up to 1800°C using sapphire tubes and inert gas to encapsulate SFBG.

It should be noted that the tubular encapsulation technique sometimes employs adhesives that might create air gaps between the protective tube and the optical fiber, leading to a loose fit and reduced structural strength of the sensor. This can cause the sensor to break easily in high temperature and high speed air flow scour environments, posing a significant risk of failure. In addition, for sapphire fiber, which has an air-clad waveguide structure, the refractive index of the adhesive must be lower than that of the sapphire to ensure effective total internal reflection of light through the fiber.

3.2. Substrate encapsulation

The tubular encapsulation technique can protect the optical fiber sensor, but it cannot be applied to the strain measurement on the structure surface. For this reason, scholars have proposed the substrate encapsulation technique. Substrate encapsulation involves attaching the optical fiber sensor to a substrate by welding or glue bonding, allowing the substrate to be welded to structural components. This technique offers several advantages, including high flexibility, good fatigue resistance, and compact structure.

In 1995, Inoue et al.[117] first proposed the use of aluminum alloy sheet to encapsulate FBG and conducted temperature sensing tests, but the sensitivity enhancement was weak. In 1996, Gupta et al.[118] successfully enhanced the temperature sensitivity of the sensor by encapsulating FBG on aluminum and polymer substrates with high CTE. The temperature sensitivity of the sensors encapsulated in the two materials was 2 to 4 times that of bare FBG, respectively. In 2005, Wnuk et al.[119] bonded FBG to a metal substrate and introduced a residual stress of −1900 με after curing of the adhesive. The sensor exhibited a linear response over the temperature measurement range of −20°C to 120°C and 1000 με. To improve the temperature range of the sensor, their team[120] subsequently bonded surface relief fiber Bragg gratings (SR-FBGs) to a metal substrate in 2006 and successfully achieved a high-temperature linear response up to 800°C. In 2009, Li et al.[121] bonded a steel tube encapsulated FBG to a semi-cylindrical metal sheet to enhance temperature sensitivity and eliminate the effect of stress. The average temperature sensitivity in the range of −15°C to 200°C reached 18.64 pm/°C. In 2014, Tu et al.[104] developed a Ni-coated RFBG fiber sensor encapsulated in a metal substrate, as shown in Fig. 12. The sensor was subjected to a uniaxial tensile test ranging from room temperature to 400°C. The results showed good strain linearity, stability, and repeatability. However, the sensor was found to be susceptible to temperature disturbance, resulting in large strain errors. Although the encapsulation
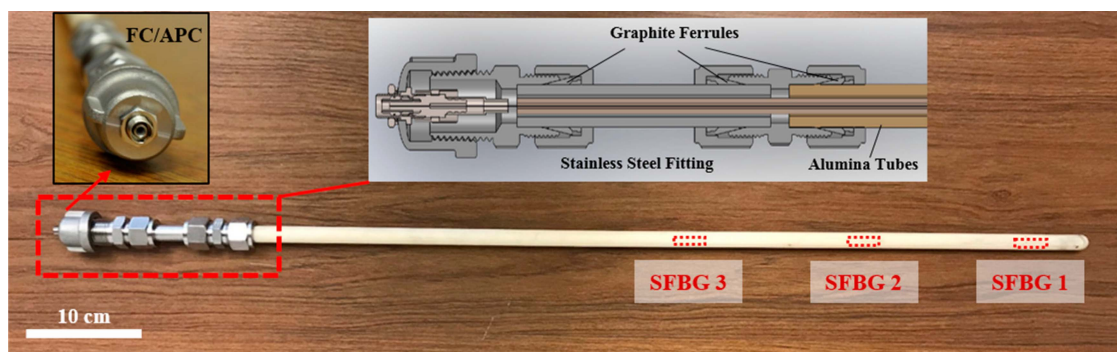

Fig. 11. Physical image of SFBG array encapsulated with sapphire tube[116].
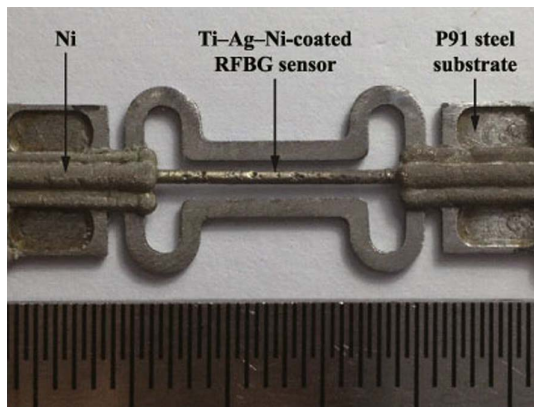
Fig. 12. Physical image of Ni-coated RFBG sensor encapsulated on steel substrate[104].

Fig. 14. Schematic diagram of stainless-steel substrate encapsulated Type-II FBG three-parameter sensor[105].

structure exhibited excellent high-temperature creep and oxidation resistance, the sensor suffered significant thermal stress at high temperatures due to the significant difference between the CTEs of the optical fiber and the metal. In addition, due to the weak mechanical strength of the RFBG, the maximum operating temperature was limited below 400°C.

In 2016, Habisreuther et al.[103] proposed a bonding encapsulation technique method for SFBG sensors. As shown in Fig. 13, the multimode SFBG high-temperature strain sensor was first encapsulated in an Inconel tube using high-temperature ceramic adhesive. Then the protective tube was bonded with high-temperature adhesive to a base steel plate with a V-shaped groove, in which the sensor was embedded. The steel plate can be welded at metal material structures to achieve high-temperature contact strain measurement. In this research, the sensor realized a temperature measurement in the range of 600°C and the strain measurement up to 1500 με.

In 2021, Yao et al.[105] designed a dual Type-II FBGs cascaded sensor with a stainless-steel substrate for high temperature, vibration, and strain measurement of structural components, the schematic diagram of which is shown in Fig. 14. The substrate bonding with the optical fiber sensor was securely fastened to the object with screws through four through-holes to enable contact measurement. FBG 1 was used for strain measurement; FBG 2 was used to measure temperature and
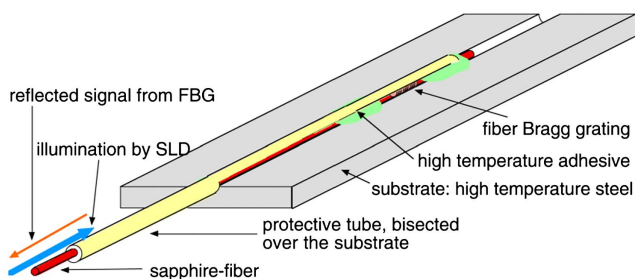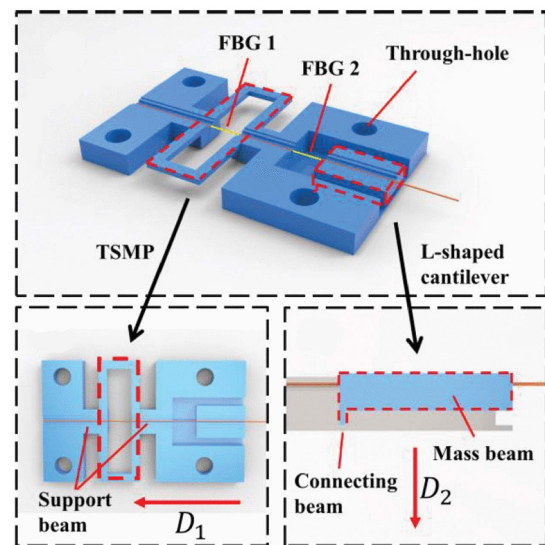
vibration, and its measurement results were used to compensate for the temperature effect of FBG 1. The sensor was capable of measuring the three parameters of temperature, strain, and vibration in the range of 1100°C, 580 με and 14 g, respectively. This sensor provides a viable solution for the engineering application of multiparameter sensing.

In summary, the substrate encapsulation technique first attaches the optical fiber sensor to the substrate by bonding or welding, and then attaches the substrate to the structural components by welding or tapped holes, thus enabling the monitoring of physical parameters of structural components. This encapsulation technique facilitates the measurement of actual physical parameters on the surface of structural components, providing high measurement accuracy and engineering applicability, However, the encapsulation technique process is achieved by bonding or welding, which cannot completely protect the entire fiber, and the mechanical properties of the bonding or welding area will be affected under high temperature, strong shock, and other environments, which may lead to sensor failure.

3.3. Metal-embedded encapsulation

In recent years, embedding optical fiber sensors directly into parts of metal materials for measurement and integration into structural components have been reported[112]. The encapsulation of embedded optical fiber sensors helps to avoid the risks associated with fiber sensors surviving in extreme environments and increases the fatigue resistance of optical fibers without compromising the integrity and thermal protection performance of the structural component. The metal-embedded encapsulation techniques can be mainly divided into three different methods: electroplating, casting, and metal 3D printing.

Fig. 13. Schematic diagram of SFBG sensors protected by metal tubes encapsulated onto a steel plate[103].

3.3.1. Electroplating

Electroplating is a low-cost and straightforward way for producing metal-embedded encapsulation, which can efficiently increase the thickness of the metal layer on the optical fiber surface and improve its fatigue resistance. To achieve a better fit between fiber and metal materials, the bare fiber needs to be surface-metallized to deposit a conductive layer before electroplating. Currently, the primary methods of fiber surface metallization include magnetron sputtering[122–124], vacuum evaporation deposition[125], and electroless plating[126]. In electroplating, the metallized optical fiber and the plated pure metal are used as cathode and anode, respectively, so that the metal cations in the solution are deposited on the surface of the optical fiber to form the plating layer.

As early as 1979, Pinnow et al.[127] applied a 15–20 μm thick aluminum coating to the fiber surface to improve the strength and fatigue resistance of the fiber. In 1989, Bubel et al.[128] used vacuum evaporation deposition to coat the fiber surface with a Ti/Pt/Au multilayer metal coating to ensure the fiber was unaffected by environmental moisture. In 2000, Watson et al.[129] used chemical plating to coat the fiber with a Ni-P alloy layer to achieve the metallization of the fiber surface. In 2006, Sandlin et al.[130] first proposed a combination of electroless plating and electroplating techniques to chemically plate silver and electroplate Ni onto an FBG for effective protection and temperature sensitivity enhancement. This sensor can operate in harsh environments up to 600°C. Normally, the metallized FBGs are solderable and can be embedded into metal structures using brazing, laser welding, ultrasonic welding, and other welding methods to monitor the physical parameters inside the structures. In 2007, Sandlin et al.[131] used a vacuum brazing method to weld Ni-plated FBG to Inconel 600 alloy, with the high temperature of the welding process reaching 900°C. The FBG survived after welding and was used for temperature measurement up to 600°C. It should be noted that the residual stress after welding was large. To eliminate possible damage to the FBG caused by the high temperature of the welding process, in 2008, Müller et al.[132] used a soft-brazing method to encapsulate the metallized FBG on the metal structure using a tin-based brazing material at a temperature of 200°C to achieve the structural health monitoring.
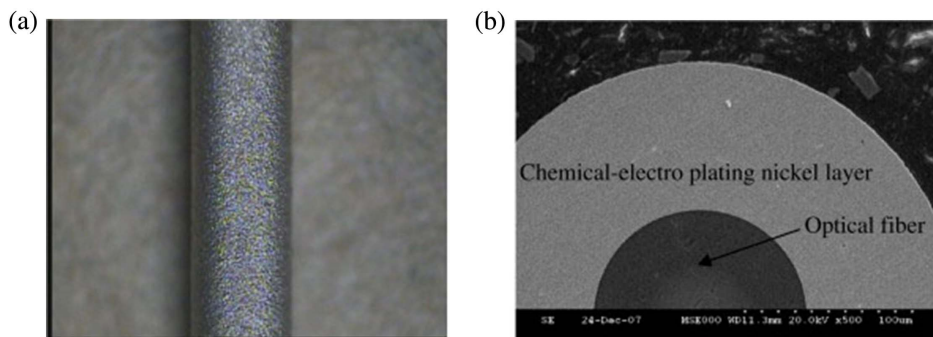
In 2009, Li et al.[109] used a combination of electroless plating and electroplating to fabricate a Ni-coated FBG temperature sensor, as shown in Fig. 15. Temperature measurements of Ni coatings with different thicknesses were performed in the range of 20°C to 300°C. The results showed that, when the coating thickness was relatively thin, the temperature sensitivity of the FBG increased rapidly with the thickness of the Ni coatings, and gradually reached a relatively stable value. In addition, the mechanism behind the increase in temperature sensitivity of FBG after metallization was theoretically analyzed, and a mathematical model of the FBG after metallization was established.

In 2014, Zheng et al.[111] used a magnetron sputtering and electroplating method to create a 22.5 μm thick iron-carbon (Fe-C) film on the surface of an FBG. The sensor was capable of monitoring corrosion for over 40 days. In 2021, Wang et al.[133] used a combination of titanium-copper (Ti-Cu) magnetron sputtering and Cu electroplating to fabricate a Ti-Cu-coated FBG temperature sensor, as shown in Fig. 16. The authors performed multiple thermal cycles in the temperature range of 79 K–293 K and conducted fatigue tests on the sensor, which failed after 560 cycles. This sensor has potential for temperature measurement in cryogenic engineering.

In 2023, Liang et al.[134] developed a high-temperature strain sensor composed of a Ni-coated FBG-FPI using electroless plating and electroplating, as shown in Fig. 17. The surface metallized fiber sensor equipped with an FBG cascaded, and an air bubble F-P cavity could measure temperature and strain simultaneously in the range of 0°C to 545°C and 0 to 1000 με. The cascaded structure reduced the impact of cross sensitivity of

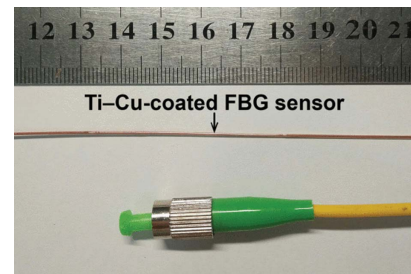**Fig. 16.** Physical image of the Ti-Cu-coated FBG temperature sensor[133].

Fig. 15. (a) Physical image of the Ni-coated fiber after plating; (b) cross section of the Ni-coated fiber[109].
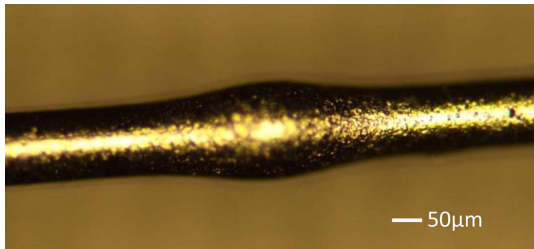
Fig. 17. Physical image of the Ni-coated FBG-FPI high-temperature strain sensors[134].

temperature and strain. The metallized optical fiber not only improves the fatigue resistance of the sensor but also enables easy integration with structural parts, thereby expanding the application range of the optical fiber sensor in structural health monitoring.

3.3.2. Casting

Optical fiber sensors can also be encapsulated or embedded into metal structures by the casting process. This method involves placing optical fibers in a casting mold prior to the casting process, where the fibers will be completely surrounded by molten metals during casting and later embedded into the solidified metal structures after cooling. This method allows for the embedding of optical fiber sensors deep within the structure, which improves their environmental adaptability while maintaining the integrity and thermal protection performance. Therefore, the embedded casting method has broad application prospects in the fields such as aviation, automotive industry, and construction, which require complex metal structures.

In 1991, Lee et al.[135] for the first time encapsulated an FPI sensor with an aluminum casting process, which could be applied for monitoring and controlling a variety of mechanical systems such as auto and aircraft, building structures, or the power plant industry. In 1998, Lin et al.[136] encapsulated an

FBG sensor with lead (solder) cladding with a casting process in an aluminum U-groove; the sensitivity of the encapsulated FBG was enhanced by ∼5 times that of a bare FBG.

Research groups from Technical University of Munich and Munich University of Applied Sciences have used FBG/RFBG sensors to monitor the high-temperature metal casting processes in the past several years. Those FBG/RFBG sensors, in direct contact with metal, could survive after the casting process with the maximum temperature of 650°C and compressive strain—10,000 µε for aluminum[31,137] and 1100°C and 14,000 µε for Cu[112]. The cast parts with embedded optical fibers were further manufactured into standard tensile test specimens to achieve tensile tests, and simultaneously temperature and strain measurement[138]. Figures 18(a) and 18(b) show the physical image and the schematic diagram of the tensile test specimen embedded with FBG sensors. Figure 18(c) shows the embedding condition of the optical fiber sensor. It can be seen that the fiber was fully surrounded by the aluminum without an obvious gap or void.

While encapsulating optical fiber sensors by the casting method has apparent advantages, such as the excellent protection due to the deep burial and the potentials for mass manufacturing and fabrication of complex structures like turbines and engines, it also presents certain challenges. The high melting points of metals, impurities in the melt during casting, and the significant contraction that occurs during the cooling process are just some of the obstacles that need to be overcome.

3.3.3. Metal 3D printing

Metal 3D printing technology can produce metal parts with complex shapes and internal structures that meet the requirements for embedded encapsulation of optical fiber sensors in various environments, including high temperature, high pressure, high-speed air scouring, and other extreme conditions. Metal 3D printing methods described in this paper mainly include laser additive manufacturing[139–141] and UAM[142–145].
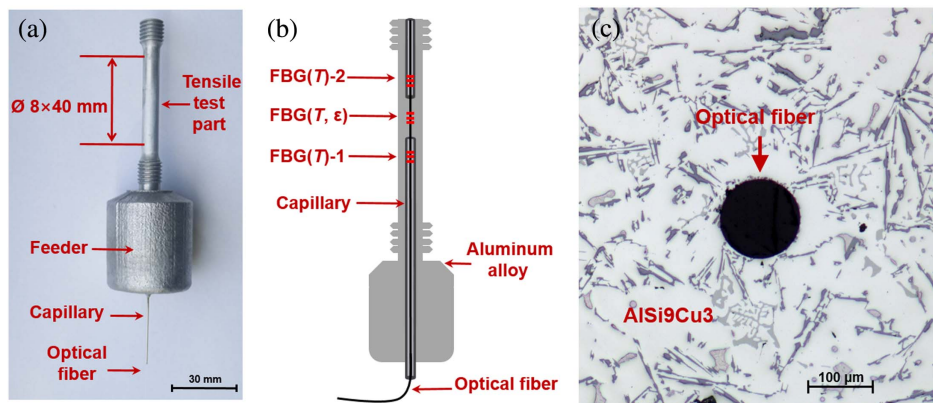

Fig. 18. Fiber-embedded aluminum specimen. (a) Physical image; (b) schematic diagram; (c) microscope image of the cross section where the fiber was in direct contact with the aluminum alloy[138].

3.3.3.1. Laser additive manufacturing

In 2002, Li et al.[146] first reported the use of laser-assisted shape deposition manufacturing (LASDM) method to embed electroplated Ni FBGs into stainless-steel structures and successfully performed 0 to 1500 µɛ strain and 0°C to 400°C temperature measurements using embedded FBG sensors. The results showed that the temperature sensitivity of the embedded FBG sensors was twice that of a bare FBG. This report demonstrates the feasibility of applying this technique for the embedded encapsulation of optical fiber sensors. Their findings have inspired many scholars to use different additive manufacturing processes to realize the embedding of optical fiber sensors. In 2011, Alemohammad et al.[147] used laser solid freeform fabrication (LSFF) method to deposit tungsten carbide-cobalt (WC-Co) layer on a Ni-electroplated FBG to achieve embedded encapsulation, and the embedded sensor maintained a linear response in the temperature range of 32.2°C to 121.7°C. In 2015, Havermann et al.[24] used selective laser melting (SLM) to embed the FBG with a thin Ni layer (~350 µm diameter) into stainless-steel 316 components; the embedded FBG exhibited a linear response in the range of 100°C to 400°C and was tested for 500 cycles of strain, a strain sensitivity of ~0.92 pm/µɛ was determined. In 2017, Zou et al.[148] used a laser-engineered net shaping (LENS) process to embed optical fiber sensors into Ti-6Al-4V assemblies. In 2017, Mathew et al.[141] used the SLM method to fabricate a high-temperature sensor consisting of an embedded metal-coated optical fiber FPI sensor, as shown in Fig. 19. The optical fiber FPI sensor was inserted into a capillary glass tube using soldering, and then silver and Ni plating was applied to allow metallization of the protective tube. Finally, the Ni-plated capillary was embedded into the SS316 stainless-steel substrate using the SLM method to achieve embedded encapsulation of the sensor. The sensor achieved the high-temperature test at 1000°C, with an accuracy better than ±10°C.

In 2020, Lei et al.[140] embedded an optical fiber IFPI temperature sensor into an Al_2O_3 substrate by CO_2 laser sintering, as shown in Fig. 20. The IFPI sensor was inserted into the substrate,
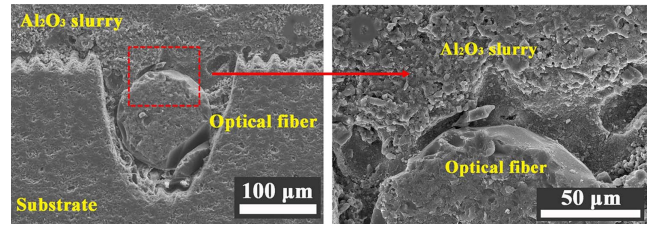
Fig. 20. Microscope picture of the cross section of the fiber IFPI sensor embedded by CO_2 laser sintering[140].

and the CO_2 laser sintering process was then used to fill the Al_2O_3 slurry, resulting in the compact encapsulation of the embedded sensor. Test results showed that the embedded IFPI sensor had long-term stability and could operate continuously for 17 h at 800°C, with a deviation of less than 10°C.

In 2022, Kim et al.[149] used a directed energy deposition (DED) process to embed a Ni-plated FBG sensor into a miniature turbine blade and monitored the structural integrity and functionality of the Ni-plated FBG sensor in situ during fabrication. The schematic diagram and the physical image of the miniature turbine blade with the Ni-FBG sensor embedded are shown in Fig. 21. The miniature turbine blade was tested for three temperature cycles in the range of 100°C to 500°C. The sensor exhibited excellent linearity, and the thermal sensitivity of the embedded FBG sensor was well-matched, with no slippage throughout the temperature monitoring. The results strongly demonstrate that the embedded optical fiber sensor is capable of high-temperature in situ monitoring of structural components and has promising applications for structural health monitoring of large structures.

The kind of laser additive manufacturing described above for embedding sensors in matrices requires operation at high temperatures, which poses a risk of transient high-temperature damage to optical fiber sensors.

3.3.3.2 Ultrasonic additive manufacturing

UAM, a solid-state additive manufacturing technology, was invented in 1999 by Dawn White[150]. UAM is a technique for creating solid metal objects by ultrasonically joining a series of metal foils into a three-dimensional structure[151]. The UAM process does not require the melting of the metal, allowing the insertion of optical fiber sensors into matrices at temperatures below 25% of the melting point of the matrix[152], thus reducing a negative impact on sensor performance due to high temperature.

In 2012, Li et al.[153] successfully embedded Ni-plated FBGs into aluminum foil using ultrasonic welding (UW) processes, and the embedded FBGs were tested at 20°C–300°C and 0–40 N tensile load on the aluminum foil; the results showed linear responses. In 2016, Zhang et al.[154] achieved the embedded encapsulation of FBG sensors in metals using UW technology. As shown in Fig. 22, the optical fiber sensor was first placed on an aluminum alloy substrate, and then used UW technology to embed the sensor into a molten indium alloy. The sensor can
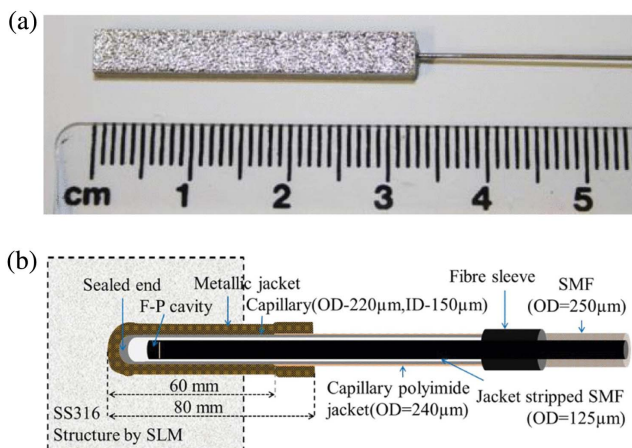

Fig. 19. (a) Physical image of the embedded high-temperature sensor made by SLM; (b) schematic diagram of the embedded FPI sensor assembly[141].
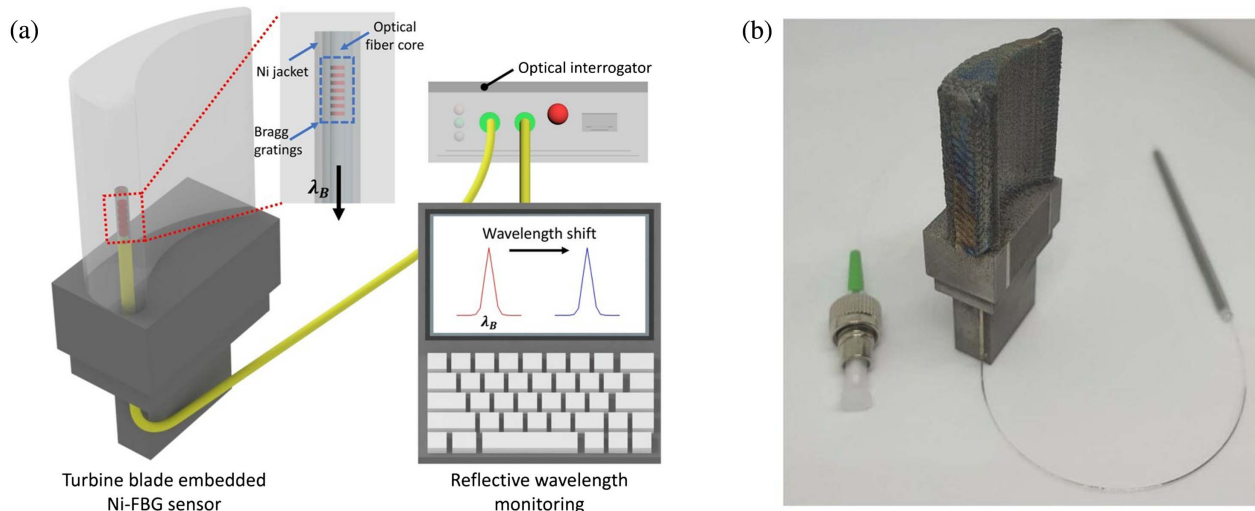
Fig. 21. (a) Schematic diagram of turbine blade with an embedded Ni-FBG sensor fabricated by DED printing for high-temperature monitoring; (b) physical image of a fully DED-printed miniature turbine blade with an embedded Ni-FBG sensor[149].
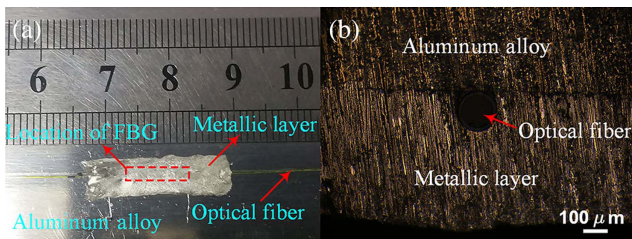

Fig. 22. (a) Physical image of metal-embedded FBG sensor on aluminum base; (b) optical micrograph of the cross section of the metal-encapsulated FBG sensor[154].

independently measure temperature and strain in the ranges of 200°C and 2000 με, and shows good linearity and stability.

In 2017, Schomer *et al.*[155] used the UAM method to embed an acrylate-coated FBG into aluminum 6061, and test results showed that the embedded FBG sensor could accurately track strain at temperatures up to 450°C. In 2019, Chilelli *et al.*[23] used UAM to embed FBG into various base specimens to fabricate temperature and strain sensors, respectively, as shown in Fig. 23. The temperature sensors were repeatedly operated at

300°C, and the strain sensors demonstrated that the embedded FBG sensors were capable of crack detection.

In 2019, Petrie *et al.*[156] used UAM to successfully embed Cu-coated, aluminum-coated, and Ni-coated fibers into an aluminum substrate, as shown in Fig. 24. After embedding, the three
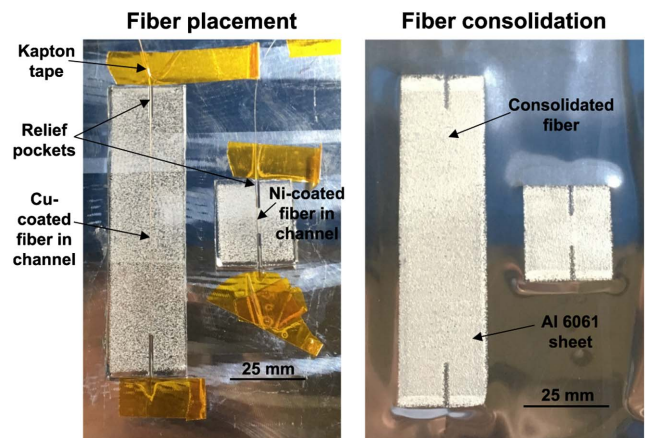

Fig. 24. Cu/Ni-plated fiber embedded in aluminum 6061-H18 substrate[156].
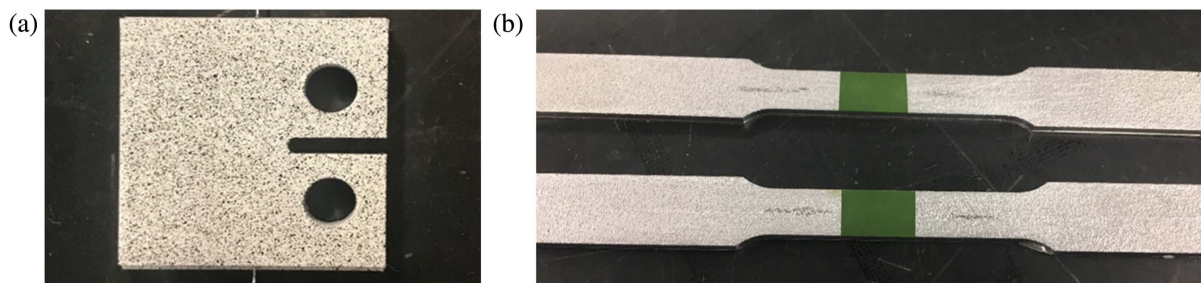

Fig. 23. (a) Embedded compact tension specimen; (b) embedded high-temperature test piece[23].

types of fibers showed good survivability at 500°C; embedding Cu-coated fibers in Cu allows for higher temperature operation.

In 2022, Hyer et al.[157] used UAM to embed optical fiber sensors into pipes and hexagonal assemblies made of stainless steel SS304 used for nuclear reactors, which were tested for distributed temperature and strain, demonstrating the potential of embedded optical fiber sensors for spatially distributed health monitoring during microreactor operation.

UAM has the advantage of low temperature manufacturing and avoids the risk of sensor failure due to high temperatures during the metal embedding encapsulation of optical fiber sensors compared to laser additive manufacturing and casting methods. However, the temperature resistance of sensors fabricated by UAM technology needs to be further improved to meet the requirements of extreme environments.

Table 4 summarizes the development of metal-embedded optical fiber sensors and lists the temperature measurement performance of embedded sensors and their different application scenarios.

4. Critical Technological Issues

4.1. Cross sensitivity between temperature and strain

Optical fiber FBG-type and FPI-type high-temperature sensors respond to both temperature and strain; therefore, when those sensors are used to monitor the temperature of structures in high temperature environments, the presence of thermal stress might affect the temperature measurement results, causing large measurement errors. At present, there are two main solutions: the dual-parameter matrix method and the temperature compensation method. The dual-parametric matrix method uses a single or multiple structures with different temperature and strain response characteristics to differentiate temperature and strain. Examples include dual Type-I FBG cascade[158], dual FPI cascade[81], dual RFBG cascade[41,159], Type-I FBG cascaded FPI[134], RFBG cascaded FPI[160,161], Type-II FBG cascaded FPI[162], cascaded dual-core PCF[163], and dual LPG cascade structures[164]. However, normally, such a dual-parameter matrix can only estimate the performance of the measurement system in a limited temperature range. In high-temperature environments, the strain sensitivity of optical fiber sensors usually varies with the ambient temperature, and the use of the dual-parameter matrix method to demodulate temperature and strain might result in large measurement error[73,165]. To address this problem, some scholars have proposed an iterative matrix algorithm[166,167], which greatly improves the accuracy of temperature and strain decoupling and the systematic error caused by the temperature dependence of the strain sensitivity. The temperature compensation method[168,169] is used to insulate one of the sensor structures from strain by encapsulation so that it only provides temperature information that can be used to compensate the temperature influence on the other structure. In addition, machine learning[170–172] has also been used to solve the problem of cross-sensitivity, and this method can achieve the

decoupling of temperature and strain with a single sensor structure, reducing the cost and complexity of the sensor system. However, its limitation is that the demodulation accuracy is not high and needs more computational power.

4.2. Material properties mismatch between metals and optical fibers

Due to the significant material differences in characteristics between metals and silica, there are mismatches in their combination. As mentioned in the previous section, there might be large gaps or defects between the metal and the embedded fiber, which greatly affects the encapsulating effect and the strain transfer between metals and optical fibers. Metal casting can achieve a better embedding condition. However, due to the significant temperature changes during the casting process and the huge difference in CTEs between the metal and silica, this process often introduces significant compressive strain, typically exceeding $-10,000~\mu\varepsilon$, under which ordinary optical fibers cannot survive after exposure to high temperatures. To solve this problem, optical fibers with larger dimensions and higher mechanical strength are used[112,137]. Additionally, it should be noted that during some encapsulation technique processes, high-temperature adhesive is used for bonding, and the mismatch in its CTE can also lead to a deterioration in the final encapsulating effect[173,174].

4.3. Sapphire fiber single-mode transmission

In recent years, extensive research about ultrahigh-temperature sensors based on sapphire fibers has been carried out. It is foreseeable that embedding sapphire fibers into metals can largely improve the upper temperature limit of the corresponding sensors. Despite their high-temperature tolerance, sapphire fibers suffer from intermode interference due to their air-clad and multimode structure. Excitation of higher-order modes will cause the SFBG reflection peak bandwidth to enlarge, and reduce the SNR and contrast of interference fringes, which seriously affects the measurement accuracy of the sensors. Therefore, reducing the number of modes in sapphire is crucial for the development of practical sapphire fiber high-temperature sensors. To address this issue, many scholars have done a great deal of research on sapphire-derived fiber (SDF)[175–178] drawing, sapphire fiber waveguide Bragg grating[179,180] fabrication, and mode field matching fusion splicing[181,182].

In 2012, Dragic et al.[175] first proposed the scheme of SDF, i.e., the SDF with a high concentration of alumina-doped glass core and silica cladding was fabricated by a drawing tower, which solved the problem of excessive modes in the sapphire fiber. In 2014, Elsmann et al.[176] inscribed Bragg gratings in SDFs using femtosecond laser processing and proved their high temperature resistance up to 950°C.

In 2017, Blue et al.[177] proposed a nearly single-mode sapphire fiber with a cladding layer and conducted high-temperature testing up to 1500°C. The sapphire fiber was placed into a ruby tube, and the gap was filled with lithium-6-rich lithium carbonate (Li_2CO_3) powder before subjecting it to irradiation in a

Table 4. Overview of Metal-Embedded Optical Fiber Sensor Embedding Methods and Applications.

| Year	Metal-Embedded Encapsulation	Optical Fiber Sensor Embedding Methods	Operating Temperature	Applications
2006[130]		Electroless plating and electroplating	Up to 600°C	High-temperature and harsh environments
2007[131]		Electroless plating, electroplating and brazing	Up to 600°C	Strain monitoring in high temperature environments
2008[132]		Conductive lacquer, electroplating and brazing		Quasi-static strain measurement
2014[111]	Electroplating	Magnetron sputtering and electroplating		Carbon steel structure corrosion monitoring
2021[133]		Magnetron sputtering and electroplating	–194°C–20°C	Temperature measurements or temperature compensation in cryogenic engineering
2023[134]		Electroless plating and electroplating	Up to 545°C	High temperature strain structural health monitoring
1991[135]		Casting aluminum	< 200°C	Monitoring and mechanical system
2018-2023[31,137]	Casting	Casting aluminum/Cu	Up to 650°C	Structural health monitoring of metallic structures
2002[146]		Magnetron sputtering, electroplating and LASDM	0°C–400°C	Structural health monitoring stainless steel structures
2011[147]		Electroplating and LSFF	32.2°C–121.7°C	Structural analysis of machining tools
2015[24]		RF sputtering, electroplating and SLM	100°C–400°C	*In situ* strain and temperature measurements inside components
2017[148]	Laser additive manufacturing	Electroplating and LENS		Measuring residual stress in additive manufacturing processes
2017[141]		Electroless plating, electroplating and SLM	Up to 1000°C	Extreme environment high temperature sensing
2020[140]		CO_2 laser sintering technology	Up to 800°C	Structural high temperature and thermal strain monitoring
2022[149]		Magnetron sputtering, electroplating and DED	100°C–500°C	Turbine blade structural health monitoring
2012[153]		Electroless plating, electroplating and UW	20°C–300°C	UW embedding processes
2016[154]		UW	50°C–200°C	Long-term and high-precision structural health monitoring
2017[155]		UAM	Up to 450°C	Structural health monitoring of metallic structures
2019[23]	UAM	UAM	Up to 300°C	Detection of crack initiation and growth
2019[156]		UAM	Up to 500°C	Structural health monitoring in harsh and high-temperature environments
2022[157]		UAM	~100°C	Distributed temperature and strain monitoring of nuclear reactors
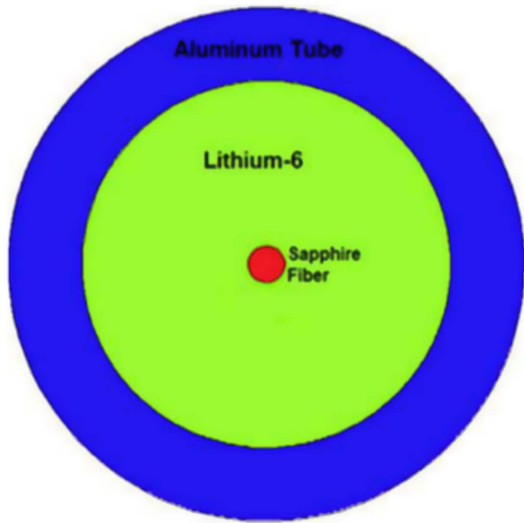
Fig. 25. Schematic diagram of Li-6 carbonate/sapphire fiber structure[177].

nuclear reactor. The resulting sapphire fiber had a cladding layer, as shown in Fig. 25. The introduction of the cladding layer enabled the sapphire fiber to achieve quasi-single-mode transmission, and the layer remained intact at temperatures up to 1500°C.

In 2019, Zhang et al.[74] fabricated a fiber-optic FPI sensor using a high-aluminum oxide-doped silica cladding SDF, and demonstrated high-temperature sensing up to 950°C and strain sensing up to 1000 με, as shown in Fig. 26. The introduction of SDF enhances the fringe contrast of IFPI.
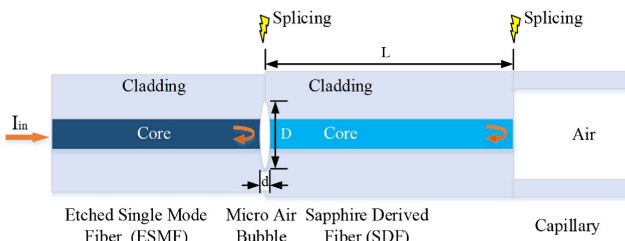

Fig. 26. Schematic diagram of the SDF-based F–P cavity structure[74].

In 2019, Liu et al.[92] used arc discharge to generate mullite particles in the SDF core region to develop SDF-FPI sensors that can withstand high temperature up to 1600°C and can operate stably at 1200°C for 6 h. In 2021, Guo et al.[178] fabricated a near-single-mode FBG with a 3 dB bandwidth of 0.33 nm on SDF and demonstrated 1000°C high-temperature sensing and up to 1100 με strain sensing.

Currently, research shows that SDF could achieve near-single-mode transmission, but the silica cladding material limits its upper temperature measurement. The arc discharge-based SDF-FPI sensor can withstand temperatures up to 1600°C[92], but can only operate stably at 1200°C. Although SDF can be manufactured from sapphire fibers with a reduced refractive index of the cladding through irradiation modification technology to achieve quasi-single-mode operation, this method requires the use of nuclear facilities such as neutron sources. Additionally, some scholars have explored using high-temperature resistant materials such as magnesium aluminate $(MgAl_2O_4)$[183], boron nitride (BN)[184], zirconium dioxide (ZrO_2)[185], and silicon boron carbon nitride (SiBCN)[186] as the cladding of sapphire fibers, but due to the higher refractive index of these materials compared to sapphire, the difference in CTE with optical fiber is too large, and the thermodynamic properties are not stable at high temperatures[187].

In 2021, Guo et al.[179] made some breakthroughs in the development of quasi-single-mode sapphire fibers. The research group inscribed a helical sapphire fiber Bragg grating (HSFBG) inside the sapphire fiber using a femtosecond laser. The HSFBG, coupled with a multimode fiber, achieved a reflectivity of 40%, a full width at half-maximum (FWHM) of 1.56 nm, and an SNR of 16 dB. The sensing capability at high temperatures below 1600°C was also demonstrated, with a temperature sensitivity of up to 35.55 pm/°C, as shown in Fig. 27. Helical gratings have structural symmetry and a large refractive index modulation region, thus reducing the excitation of higher-order modes by the increased length of the sapphire fiber and the presence of surface defects. This study indicates that the helical fiber grating can suppress the transmission of high-order modes, thereby improving the system's SNR. However, a multimode fiber is still required to obtain stable spectra.
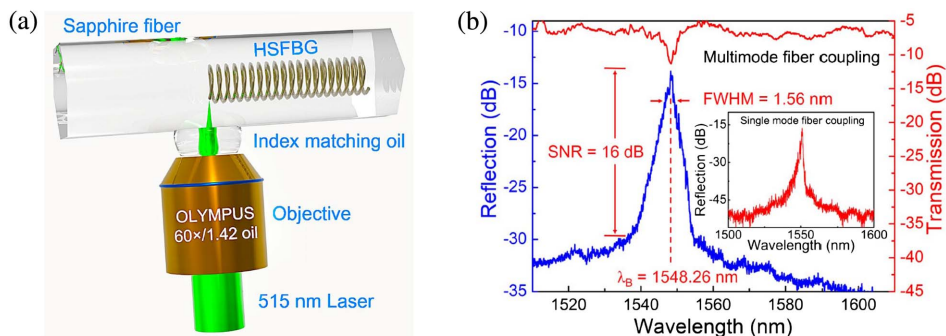

Fig. 27. (a) Experimental setup of HSFBGs inscribed in a sapphire fiber; (b) HSFBG reflection and transmission spectra of multimode fiber coupling. The illustration is the reflection spectrum of HSFBG with SMF coupling[179].
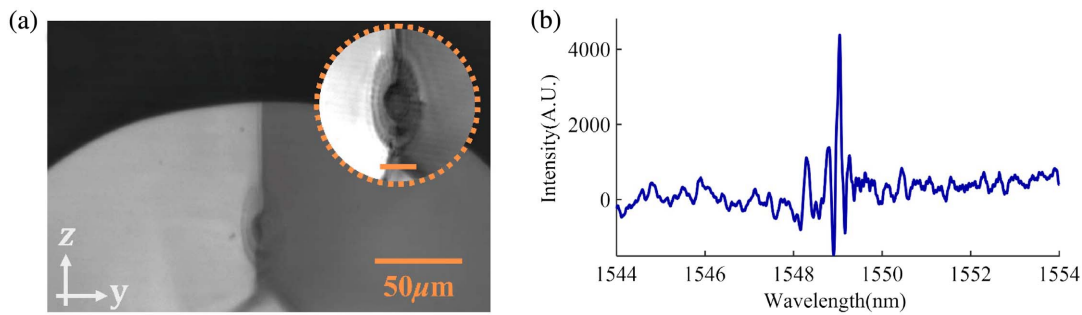
Fig. 28. (a) Microscope image of the SFBG; (b) SFBG reflection spectrum[180].

In 2022, Wang *et al.*[180] created a depressed cladding wave-guide (DCW) on a sapphire fiber and inscribed a ring-shaped FBG inside it, resulting in a single-mode SFBG with a reflection peak bandwidth of less than 0.5 nm. The FBG could survive even after annealing at 1000°C, as shown in Fig. 28. The DCW structure enabled single-mode transmission on both bulk sapphire and sapphire fibers. This study provided a technological framework for the development of single-mode sapphire fibers based on femtosecond laser processing, but its insertion loss is greater than 6.8 dB/cm, so this method can

only be used to manufacture single-mode SFBG with centimeter-level length.

In 2022, Jones *et al.*[181] made some progress in developing a single-mode sapphire fiber system by using direct fusion splicing technology to control the tapering of the fusion zone and achieve filtering of higher-order modes in the sapphire fiber. This has resulted in the conversion of the sapphire fiber system to a single-mode one. A physical image of the fusion splice region is shown in Fig. 29. These findings provide valuable insights into the development of single-mode sapphire fiber systems.
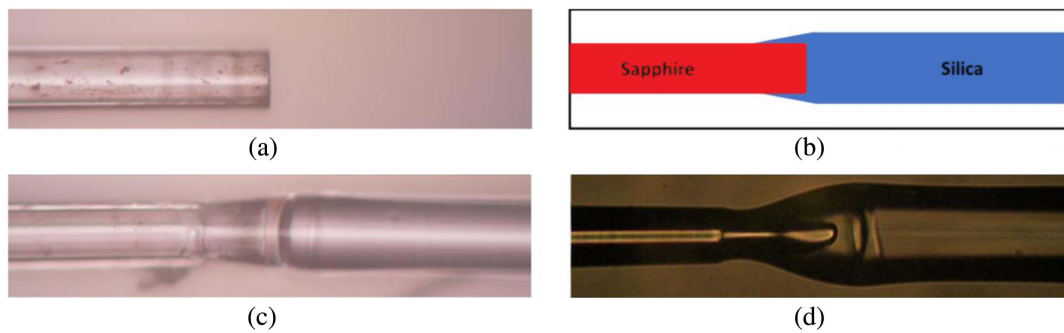

Fig. 29. (a) Polished sapphire end face; (b) schematic of fusion bonding; (c) successful fusion; (d) failed fusion[181].
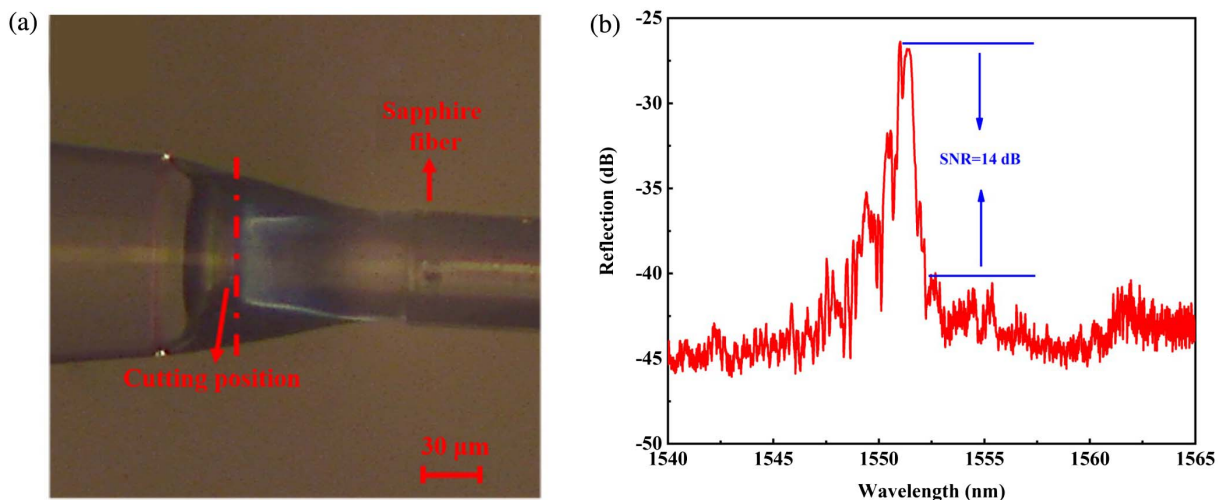

Fig. 30. (a) Microscope image of overlapped double conical splicing region between the sapphire fiber (Φ60 μm) and SMF-28e+; (b) SFBG reflection spectrum obtained by using pretapered SMF for splicing[182].

In cooperation with Shenzhen University, recently, our research group[188] has proposed a fusion splicing method based on mode field matching to suppress the high-order modes in SFBGs. An overlapped double conical splicing structure between sapphire fiber and SMF was formed, as shown in Fig. 30(a). A quasi-single mode reflection spectrum from SFBG was obtained based on this method with an FWHM of 0.3 nm and an SNR of 8 dB. Further improvement has been made on this fusion splicing method by using a pretapered SMF; the SNR reached 14 dB, as shown in Fig. 30(b). In addition, the SFBG sensor was further combined with a commercial single-mode interrogator and achieved a real-time temperature monitoring up to 1160°C.

Despite considerable progress made by many research groups in the field of single-mode transmission of sapphire fibers, there is still no SFBG sensor with quasi-single-mode spectrum that can withstand testing above 1300°C. Research on SFBG sensors remains at the experimental stage, and commercial products suitable for practical use in extreme environments have yet to be reported.

5. Conclusion

This paper presents the research progress of FBG-type and FPI-type high-temperature sensors. Temperature measurement capability and defects of silica-based fiber high-temperature sensors have been reviewed, and temperature sensing performance of sensors based on sapphire fiber has been summarized. The research progress of the encapsulation technique for fiber high-temperature sensors is comprehensively discussed. Different encapsulation technique methods are compared and analyzed in terms of their ability to ensure sensor consistency and enhance extreme environment adaptability.

Metal-embedded fiber sensors are found to be capable of monitoring the structural health of high-end manufacturing equipment such as engines under extreme conditions while enhancing fiber fatigue resistance without compromising structural integrity and thermal protection. Despite the significant breakthroughs achieved in the upper temperature limit and encapsulation technique aspects of fiber sensors, there are still many technical challenges that need to be addressed, such as the cross sensitivity between temperature and strain, the material properties mismatch between metals and optical fibers that might lead to insufficient sensor reliability, and how to suppress sapphire fiber high-order modes to obtain SFBG sensors that can be applied in practical environments.

Acknowledgement

References

1. H. Xia, D. Byrd, S. Dekate, and B. Lee, "High-density fiber optical sensor and instrumentation for gas turbine operation condition monitoring," J. Sens. **2013**, 206738 (2013).
2. Y. S. H. Najjar and I. A. I. Balawneh, "Optimization of gas turbines for sustainable turbojet propulsion," Propuls. Power Res. **4**, 114 (2015).
3. W. Ma, Y. Jiang, and H. Gao, "Miniature all-fiber extrinsic Fabry–Pérot interferometric sensor for high-pressure sensing under high-temperature conditions," Meas. Sci. Technol. **30**, 025104 (2019).
4. M. Chen, H. Qiu, W. Xie, B. Zhang, S. Liu, W. Luo, and X. Ma, "Research progress of continuous fiber reinforced ceramic matrix composite in hot section components of aero engine," IOP Conf. Ser. Mater. Sci. Eng. **678**, 012043 (2019).
5. T. Bosselmann, "Innovative applications of fibre-optic sensors in energy and transportation [Invited Paper]," Proc. SPIE **5855**, 188 (2005).
6. L. Polz, A. Zeisberger, H. Bartelt, and J. Roths, "Total temperature measurement of fast air streams with fiber-optic Bragg grating sensors," IEEE Sens. J. **16**, 6596 (2016).
7. K. M. Pandey, G. Choubey, F. Ahmed, D. H. Laskar, and P. Ramnani, "Effect of variation of hydrogen injection pressure and inlet air temperature on the flow-field of a typical double cavity scramjet combustor," Int. J. Hydrog. Energy **42**, 20824 (2017).
8. Y. Tian, S. Yang, J. Le, T. Su, M. Yue, F. Zhong, and X. Tian, "Investigation of combustion and flame stabilization modes in a hydrogen fueled scramjet combustor," Int. J. Hydrog. Energy **41**, 19218 (2016).
9. J. Urzay, "Supersonic combustion in air-breathing propulsion systems for hypersonic flight," Annu. Rev. Fluid Mech. **50**, 593 (2018).
10. A. Purwar and S. Deep, "A novel thermocouple for ultra high temperature applications: design and computational analysis," in *IEEE International Conference on Consumer Electronics-Asia (ICCE-Asia)* (2017), p. 145.
11. H.-N. Li, D.-S. Li, and G.-B. Song, "Recent applications of fiber optic sensors to health monitoring in civil engineering," Eng. Struct. **26**, 1647 (2004).
12. W. Li, T. Liang, P. Jia, C. Lei, Y. Hong, Y. Li, Z. Yao, W. Liu, and J. Xiong, "Fiber-optic Fabry-Perot pressure sensor based on sapphire direct bonding for high-temperature applications," Appl. Opt. **58**, 1662 (2019).
13. J. Deng and D. N. Wang, "Construction of cascaded Fabry-Perot interferometers by four in-fiber mirrors for high-temperature sensing," Opt. Lett. **44**, 1289 (2019).
14. C. R. Liao and D. N. Wang, "Review of femtosecond laser fabricated fiber Bragg gratings for high temperature sensing," Photonic Sens. **3**, 97 (2012).
15. H. Xiao, J. Deng, G. Pickrell, R. G. May, and A. Wang, "Single-crystal sapphire fiber-based strain sensor for high-temperature applications," J. Lightwave Technol. **21**, 2276 (2003).
16. D. Grobnic, S. J. Mihailov, C. W. Smelser, and H. Ding, "Sapphire fiber Bragg grating sensor made using femtosecond laser radiation for ultrahigh temperature applications," IEEE Photon. Technol. Lett. **16**, 2505 (2004).
17. M. Busch, W. Ecke, I. Latka, D. Fischer, R. Willsch, and H. Bartelt, "Inscription and characterization of Bragg gratings in single-crystal sapphire optical fibres for high-temperature sensor applications," Meas. Sci. Technol. **20**, 115301 (2009).
18. S. Yang, D. Hu, and A. Wang, "Point-by-point fabrication and characterization of sapphire fiber Bragg gratings," Opt. Lett. **42**, 4219 (2017).
19. Y. Tu, Y.-K. Huang, and S.-T. Tu, "Real-time monitoring of bolt clamping force at high temperatures using metal-packaged regenerated fiber Bragg grating sensors," Int. J. Press. Vessels Pip. **172**, 119 (2019).
20. Y.-L. Wang, Y. Tu, and S.-T. Tu, "A study of tensile and fatigue loading effects on the performance of metal-packaged FBG strain sensor developed for cryogenic applications," IEEE Sens. J. **22**, 11763 (2022).
21. M. Lindner, A. Stadler, G. Hamann, B. Fischer, M. Jakobi, F. Heilmeier, C. Bauer, W. Volk, A. W. Koch, and J. Roths, "Fiber Bragg sensors embedded in cast aluminum parts: axial strain and temperature response," Sensors **21**, 1680 (2021).

22. F. Heilmeier, R. Koos, K. Weraneck, M. Lindner, M. Jakobi, J. Roths, A. W. Koch, and W. Volk, "In-situ strain measurements in the plastic deformation regime inside casted parts using fibre-optical strain sensors," Prod. Eng. **13**, 351 (2019).

23. S. K. Chilelli, J. J. Schomer, and M. J. Dapino, "Detection of crack initiation and growth using fiber Bragg grating sensors embedded into metal structures through ultrasonic additive manufacturing," Sensors **19**, 4917 (2019).

24. D. Havermann, J. Mathew, W. N. MacPherson, R. R. J. Maier, and D. P. Hand, "Temperature and strain measurements with fiber Bragg gratings embedded in stainless steel 316," J. Lightwave Technol. **33**, 2474 (2015).

25. C. Lupi, F. Felli, A. dell'Era, E. Ciro, M. A. Caponero, H. J. Kalinowski, and C. Vendittozzi, "Critical issues of double-metal layer coating on FBG for applications at high temperatures," Sensors **19**, 3824 (2019).

26. R. R. Dils, "High-temperature optical fiber thermometer," J. Appl. Phys. **54**, 1198 (1983).

27. D. Liu, Y. Duan, and Z. Yang, "Integrated ef fective emissivity computation for non-isothermal non-axisymmetric cavities," Chin. Opt. Lett. **11**, 022001 (2013).

28. Y. Guo, W. Xia, Z. Hu, and M. Wang, "High-temperature sensor instrumentation with a thin-film-based sapphire fiber," Appl. Opt. **56**, 2068 (2017).

29. W. Wei, S. Xiaotian, and W. Ying, "Sapphire fiber-optic temperature sensor based on black-body radiation law," Procedia Eng. **99**, 1179 (2015).

30. A. Othonos, "Fiber Bragg gratings," Rev. Sci. Instrum. **68**, 4309 (1997).

31. M. Lindner, E. Tunc, K. Weraneck, F. Heilmeier, W. Volk, M. Jakobi, A. W. Koch, and J. Roths, "Regenerated Bragg grating sensor array for temperature measurements during an aluminum casting process," IEEE Sens. J. **18**, 5352 (2018).

32. K. O. Hill, Y. Fujii, D. C. Johnson, and B. S. Kawasaki, "Photosensitivity in optical fiber waveguides: application to reflection filter fabrication," Appl. Phys. Lett. **32**, 647 (1978).

33. T. Erdogan, V. Mizrahi, P. J. Lemaire, and D. Monroe, "Decay of ultraviolet-induced fiber Bragg gratings," J. Appl. Phys. **76**, 73 (1994).

34. Y. Huang, Z. Zhou, Y. Zhang, G. Chen, and H. Xiao, "A temperature self-compensated LPFG sensor for large strain measurements at high temperature," IEEE Trans. Instrum. Meas. **59**, 2997 (2010).

35. J. Canning, M. Stevenson, S. Bandyopadhyay, and K. Cook, "Extreme silica optical fibre gratings," Sensors **8**, 6448 (2008).

36. Y. Zhu, H. Mei, T. Zhu, J. Zhang, and S. Yin, "Dual-wavelength FBG inscribed by femtosecond laser for simultaneous measurement of high temperature and strain," Chin. Opt. Lett. **7**, 675 (2009).

37. F. J. Dutz, A. Heinrich, R. Bank, A. W. Koch, and J. Roths, "Fiber-optic multipoint sensor system with low drift for the long-term monitoring of high-temperature distributions in chemical reactors," Sensors **19**, 5476 (2019).

38. G. Laffont, R. Cotillard, N. Roussel, R. Desmarchelier, and S. Rougeault, "Temperature resistant fiber bragg gratings for on-line and structural health monitoring of the next-generation of nuclear reactors," Sensors **18**, 1791 (2018).

39. L. Polz, F. J. Dutz, R. R. J. Maier, H. Bartelt, and J. Roths, "Regenerated fibre Bragg gratings: a critical assessment of more than 20 years of investigations," Opt. Laser Technol. **134**, 106650 (2021).

40. M. A. Fokine, B. E. Sahlgren, and R. Stubbe, "A novel approach to fabricate high-temperature resistant fiber Bragg gratings," in *Bragg Gratings, Photosensitivity, and Poling in Glass Fibers and Waveguides* (1997), paper. BSuD.5.

41. H. Z. Yang, X. G. Qiao, Y. P. Wang, M. M. Ali, M. H. Lai, K. S. Lim, and H. Ahmad, "In-fiber gratings for simultaneous monitoring temperature and strain in ultrahigh temperature," IEEE Photon. Technol. Lett. **27**, 58 (2015).

42. D. S. Gunawardena, O. K. Law, Z. Liu, X. Zhong, Y. T. Ho, and H. Y. Tam, "Resurgent regenerated fiber Bragg gratings and thermal annealing techniques for ultra-high temperature sensing beyond 1400°C," Opt. Express **28**, 10595 (2020).

43. P. Rinaudo, B. Torres, I. Paya-Zaforteza, P. A. Calderón, and S. Sales, "Evaluation of new regenerated fiber Bragg grating high-temperature sensors in an ISO 834 fire test," Fire Saf. J. **71**, 332 (2015).

44. F. J. Dutz, M. Lindner, A. Heinrich, C. G. Seydel, T. Bosselmann, A. W. Koch, and J. Roths, "Multipoint high temperature sensing with regenerated fiber Bragg gratings," Proc. SPIE **10654**, 1065407 (2018).

45. J. L. Archambault, L. Reekie, and P. St.J. Russell, "100% reflectivity Bragg reflectors produced in optical fibres by single excimer laser pulses," Electron. Lett. **29**, 453 (1993).

46. A. Martinez, M. Dubov, I. Khrushchev, and I. Bennion, "Direct writing of fibre Bragg gratings by femtosecond laser," Electron. Lett. **40**, 1170 (2004).

47. D. Grobnic, C. W. Smelser, S. J. Mihailov, and R. B. Walker, "Long-term thermal stability tests at 1000°C of silica fibre Bragg gratings made with ultrafast laser radiation," Meas. Sci. Technol. **17**, 1009 (2006).

48. Y. Li, M. Yang, C. Liao, D. Wang, J. Lu, and P. Lu, "Prestressed fiber Bragg grating with high temperature stability," J. Lightwave Technol. **29**, 1555 (2011).

49. S. C. Warren-Smith, E. P. Schartner, L. V. Nguyen, D. E. Otten, Z. Yu, D. G. Lancaster, and H. Ebendorff-Heidepriem, "Stability of grating-based optical fiber sensors at high temperature," IEEE Sens. J. **19**, 2978 (2019).

50. D. Grobnic, C. Hnatovsky, S. Dedyulin, R. B. Walker, H. Ding, and S. J. Mihailov, "Fiber Bragg grating wavelength drift in long-term high temperature annealing," Sensors **21**, 1454 (2021).

51. R. B. Walker, S. Yun, M. De Silva, N. Charest, C. Hnatovsky, P. Lu, D. Robertson, S. J. Mihailov, and P. Vena, "High temperature measurement of a low emission, high pressure combustor using femtosecond laser written fiber Bragg gratings," Proc. SPIE **10654**, 1065408 (2018).

52. M. A. S. Zaghloul, M. Wang, S. Huang, C. Hnatovsky, D. Grobnic, S. Mihailov, M. J. Li, D. Carpenter, L. W. Hu, J. Daw, G. Laffont, S. Nehr, and K. P. Chen, "Radiation resistant fiber Bragg grating in random air-line fibers for sensing applications in nuclear reactor cores," Opt. Express **26**, 11775 (2018).

53. J. Yao, L. Ye, Y. Ishii, Z. Shen, L. Tong, and Y. Shen, "Optical properties of sapphire fiber under high temperature," Proc. SPIE **4919**, 161 (2002).

54. S. Yang, D. Hu, and A. Wang, "Point-by-point fabrication and characterization of sapphire fiber Bragg gratings," Opt. Lett. **42**, 4219 (2017).

55. X. Xu, J. He, C. Liao, K. Yang, K. Guo, C. Li, Y. Zhang, Z. Ouyang, and Y. Wang, "Sapphire fiber Bragg gratings inscribed with a femtosecond laser line-by-line scanning technique," Opt. Lett. **43**, 4562 (2018).

56. D. Grobnic, S. J. Mihailov, H. Ding, F. Bilodeau, and C. W. Smelser, "Single and low order mode interrogation of a multimode sapphire fibre Bragg grating sensor with tapered fibres," Meas. Sci. Technol. **17**, 980 (2006).

57. M. Busch, W. Ecke, I. Latka, D. Fischer, R. Willsch, and H. Bartelt, "Inscription and characterization of Bragg gratings in single-crystal sapphire optical fibres for high-temperature sensor applications," Meas. Sci. Technol. **20**, 115301 (2009).

58. T. Habisreuther, T. Elsmann, Z. Pan, A. Graf, R. Willsch, and M. A. Schmidt, "Sapphire fiber Bragg gratings for high temperature and dynamic temperature diagnostics," Appl. Therm. Eng. **91**, 860 (2015).

59. J. He, X. Xu, B. Du, B. Xu, R. Chen, Y. Wang, C. Liao, J. Guo, Y. Wang, and J. He, "Stabilized ultra-high-temperature sensors based on inert gas-sealed sapphire fiber Bragg gratings," ACS Appl. Mater. Interfaces **14**, 12359 (2022).

60. J. Canning, "Fibre gratings and devices for sensors and lasers," Laser Photonics Rev. **2**, 275 (2008).

61. G. Meltz, W. W. Morey, and W. H. Glenn, "Formation of Bragg gratings in optical fibers by a transverse holographic method," Opt. Lett. **14**, 823 (1989).

62. B. Dong, L. Wei, and D.-P. Zhou, "Miniature high-sensitivity high-temperature fiber sensor with a dispersion compensation fiber-based interferometer," Appl. Opt. **48**, 6466 (2009).

63. X. Tan, Y. Geng, X. Li, R. Gao, and Z. Yin, "High temperature microstructured fiber sensor based on a partial-reflection-enabled intrinsic Fabry-Perot interferometer," Appl. Opt. **52**, 8195 (2013).

64. Y. Du, X. Qiao, Q. Rong, H. Yang, D. Feng, R. Wang, M. Hu, and Z. Feng, "A miniature Fabry–Pérot interferometer for high temperature measurement using a double-core photonic crystal fiber," IEEE Sens. J. **14**, 1069 (2014).

65. W. Ding, Y. Jiang, R. Gao, and Y. Liu, "High-temperature fiber-optic Fabry-Perot interferometric sensors," Rev. Sci. Instrum. **86**, 055001 (2015).

66. Z. Chen, S. Xiong, S. Gao, H. Zhang, L. Wan, X. Huang, B. Huang, Y. Feng, W. Liu, and Z. Li, "High-temperature sensor based on Fabry-Perot interferometer in microfiber tip," Sensors **18**, 202 (2018).

67. Q. Wang, H. Zhang, and D. N. Wang, "Cascaded multiple Fabry-Perot interferometers fabricated in no-core fiber with a waveguide for high-temperature sensing," Opt. Lett. **44**, 5145 (2019).

68. G. Zhang, X. Wu, S. Li, W. Liu, S. Fang, C. Zuo, W. Zhang, and B. Yu, "Miniaturized Fabry-Perot probe utilizing PMPCF for high temperature measurement," Appl. Opt. **59**, 873 (2020).

69. P. Xia, Y. Tan, C. Yang, Z. Zhou, and K. Yun, "A composite Fabry-Perot interferometric sensor with the dual-cavity structure for simultaneous measurement of high temperature and strain," Sensors **21**, 4989 (2021).

70. Y. Han, B. Liu, Y. Wu, Y. Mao, J. Wu, L. Zhao, T. Nan, J. Wang, R. Tang, and Y. Zhang, "High-sensitivity transverse-load and high-temperature sensor based on the cascaded Vernier effect," Appl. Opt. **60**, 7714 (2021).

71. P. A. R. Tafulo, P. A. S. Jorge, J. L. Santos, and O. Frazão, "Fabry–Pérot cavities based on chemical etching for high temperature and strain measurement," Opt. Commun. **285**, 1159 (2012).

72. A. Kaur, S. E. Watkins, J. Huang, L. Yuan, and H. Xiao, "Microcavity strain sensor for high temperature applications," Opt. Eng. **53**, 017105 (2014).

73. Y. Jiang, D. Yang, Y. Yuan, J. Xu, D. Li, and J. Zhao, "Strain and high-temperature discrimination using a Type II fiber Bragg grating and a miniature fiber Fabry-Perot interferometer," Appl. Opt. **55**, 6341 (2016).

74. P. Zhang, L. Zhang, Z. Wang, X. Zhang, and Z. Shang, "Sapphire derived fiber based Fabry-Perot interferometer with an etched micro air cavity for strain measurement at high temperatures," Opt. Express **27**, 27112 (2019).

75. J. Nan, D. Zhang, X. Wen, M. Li, H. Lv, and K. Su, "Elimination of thermal strain interference in mechanical strain measurement at high temperature using an EFPI-RFBG hybrid sensor with unlimited cavity length," IEEE Sens. J. **20**, 5270 (2020).

76. X. Liu, P. Nan, J. Zhu, Z. Li, J. Dan, W. Dang, K.-S. Lim, W. Udos, H. Ahmad, and X. Liu, "Ultrasensitive parallel double-FPIs sensor based on Vernier effect and Type II fiber Bragg grating for simultaneous measurement of high temperature and strain," Opt. Commun. **508**, 127717 (2022).

77. Y. Hu, H. Wei, Z. Ma, L. Zhang, F. Pang, and T. Wang, "Microbubble-based optical fiber Fabry-Perot sensor for simultaneous high-pressure and high-temperature sensing," Opt. Express **30**, 33639 (2022).

78. Z. Li, W. Dang, J. Dan, K. Jin, P. Nan, G. Xin, K.-S. Lim, H. Ahmad, and H. Yang, "High-sensitivity interferometric high-temperature strain sensor based on optical harmonic Vernier effect," Opt. Fiber Technol. **79**, 103361 (2023).

79. X. L. Cui, H. Zhang, and D. N. Wang, "Parallel structured optical fiber in-line Fabry-Perot interferometers for high temperature sensing," Opt. Lett. **45**, 726 (2020).

80. Z. Wang, H. Liu, Z. Ma, Z. Chen, T. Wang, and F. Pang, "High temperature strain sensing with alumina ceramic derived fiber based Fabry-Perot interferometer," Opt. Express **27**, 27691 (2019).

81. T. Paixao, F. Araujo, and P. Antunes, "Highly sensitive fiber optic temperature and strain sensor based on an intrinsic Fabry-Perot interferometer fabricated by a femtosecond laser," Opt. Lett. **44**, 4833 (2019).

82. G. C. Fang, P. G. Jia, Q. Cao, and J. J. Xiong, "MEMS fiber-optic Fabry-Perot pressure sensor for high temperature application," Proc. SPIE **10155**, 101552H (2016).

83. W. Wang, W. Wu, S. Wu, Y. Li, C. Huang, X. Tian, X. Fei, and J. Huang, "Adhesive-free bonding homogenous fused-silica Fabry–Perot optical fiber low pressure sensor in harsh environments by CO_2 laser welding," Opt. Commun. **435**, 97 (2019).

84. T. Yoshino, K. Kurosawa, K. Itoh, and T. Ose, "Fiber-optic Fabry-Perot interferometer and its sensor applications," IEEE Trans. Microw. Theory Tech. **30**, 1612 (1982).

85. C. E. Lee and H. F. Taylor, "Fiber-optic Fabry-Perot temperature sensor using a low-coherence light source," J. Lightwave Technol. **9**, 129 (1991).

86. H. Y. Choi, K. S. Park, S. J. Park, U. C. Paek, B. H. Lee, and E. S. Choi, "Miniature fiber-optic high temperature sensor based on a hybrid structured Fabry-Perot interferometer," Opt. Lett. **33**, 2455 (2008).

87. T. Wei, Y. Han, H.-L. Tsai, and H. Xiao, "Miniaturized fiber inline Fabry-Perot interferometer fabricated with a femtosecond laser," Opt. Lett. **33**, 536 (2008).

88. X. Lei, X. Dong, B. Zagar, P. Mazurek, M. Rosenberger, and P.-G. Dittrich, "Sensitivity-enhanced fiber interferometric high temperature sensor based on Vernier effect," Proc. SPIE **11144**, 1114405 (2019).

89. X. Lei and X. Dong, "High-sensitivity Fabry–Perot interferometer high-temperature fiber sensor based on Vernier effect," IEEE Sens. J. **20**, 5292 (2020).

90. J. Wang, E. M. Lally, B. Dong, J. Gong, and A. Wang, "Fabrication of a miniaturized thin-film temperature sensor on a sapphire fiber tip," IEEE Sens. J. **11**, 3406 (2011).

91. H. Xiao, J. Deng, G. Pickrell, R. G. May, and A. Wang, "Single-crystal sapphire fiber-based strain sensor for high-temperature applications," J. Lightwave Technol. **21**, 2276 (2003).

92. H. Liu, F. Pang, L. Hong, Z. Ma, L. Huang, Z. Wang, J. Wen, Z. Chen, and T. Wang, "Crystallization-induced refractive index modulation on sapphire-derived fiber for ultrahigh temperature sensing," Opt. Express **27**, 6201 (2019).

93. A. Wang, S. Gollapudi, K. A. Murphy, R. G. May, and R. O. Claus, "Sapphire-fiber-based intrinsic Fabry–Perot interferometer," Opt. Lett. **17**, 1021 (1992).

94. Y. Zhu and A. Wang, "Surface-mount sapphire interferometric temperature sensor," Appl. Opt. **45**, 6071 (2006).

95. X. Yu, S. Wang, J. Jiang, K. Liu, Z. Wu, and T. Liu, "Self-filtering high-resolution dual-sapphire-fiber-based high-temperature sensor," J. Lightwave Technol. **37**, 1408 (2019).

96. S. Yang, Z. Feng, X. Jia, G. Pickrell, W. Ng, A. Wang, and Y. Zhu, "All-sapphire miniature optical fiber tip sensor for high temperature measurement," J. Lightwave Technol. **38**, 1988 (2020).

97. P. S. Reddy, "Encapsulated fiber Bragg grating sensor for high temperature measurements," Opt. Eng. **50**, 114401 (2011).

98. N. J. Lawson, R. Correia, S. W. James, M. Partridge, S. E. Staines, J. E. Gautrey, K. P. Garry, J. C. Holt, and R. P. Tatam, "Development and application of optical fibre strain and pressure sensors for in-flight measurements," Meas. Sci. Technol. **27**, 104001 (2016).

99. B. Wang, Y. Niu, S. Zheng, Y. Yin, and M. Ding, "A high temperature sensor based on sapphire fiber Fabry-Perot interferometer," IEEE Photon. Technol. Lett. **32**, 89 (2020).

100. V. R. Mamidi, S. Kamineni, L. N. S. P. Ravinuthala, M. Martha, S. S. Madhuvarasu, and V. R. Thumu, "High-temperature measurement using fiber Bragg grating sensor accompanied by a low-cost detection system," J. Appl. Remote Sens. **9**, 094098 (2015).

101. P. Xia, Y. Tan, T. Li, Z. Zhou, and W. Lv, "A high-temperature resistant photonic crystal fiber sensor with single-side sliding Fabry-Perot cavity for super-large strain measurement," Sens. Actuators A **318**, 112492 (2021).

102. P. Chen, Y. Wu, and Y. Wang, "Optical fiber Fabry-Perot temperature sensor based on metal welding technology," J. Nanophotonics **17**, 026001 (2023).

103. T. Habisreuther, T. Elsmann, A. Graf, and M. A. Schmidt, "High-temperature strain sensing using sapphire fibers with inscribed first-order Bragg gratings," IEEE Photon. J. **8**, 1 (2016).

104. Y. Tu and S.-T. Tu, "Fabrication and characterization of a metal-packaged regenerated fiber Bragg grating strain sensor for structural integrity monitoring of high-temperature components," Smart Mater. Struct. **23**, 035001 (2014).

105. K. Yao, Q. Lin, Z. Jiang, N. Zhao, B. Tian, and G.-D. Peng, "Design and analysis of a combined FBG Sensor for the measurement of three parameters," IEEE Trans. Instrum. Meas. **70**, 7003010 (2021).

106. C. M. Petrie, N. Sridharan, A. Hehr, M. Norfolk, and J. Sheridan, "High-temperature strain monitoring of stainless steel using fiber optics embedded in ultrasonically consolidated nickel layers," Smart Mater. Struct. **28**, 085041 (2019).

107. C. Lupi, F. Felli, A. Brotzu, M. A. Caponero, and A. Paolozzi, "Improving FBG sensor sensitivity at cryogenic temperature by metal coating," IEEE Sens. J. **8**, 1299 (2008).

108. S. Li, Y. Li, X. Liu, X. Li, T. Ding, and H. Ouyang, "An in-situ electroplating fabricated Fabry-Perot interferometric sensor and its temperature sensing characteristics," Coatings **10**, 1174 (2020).

109. Y. Li, Z. Hua, F. Yan, and P. Gang, "Metal coating of fiber Bragg grating and the temperature sensing character after metallization," Opt. Fiber Technol. **15**, 391 (2009).

110. Y. Li, H. Zhang, Y. Feng, and G. Peng, "A plating method for metal coating of fiber Bragg grating," Chin. Opt. Lett. **7**, 115 (2009).

111. X. Zheng, W. Hu, N. Zhang, and M. Gao, "Optical corrosion sensor based on fiber Bragg grating electroplated with Fe-C film," Opt. Eng. **53**, 077104 (2014).

112. Q. Bian, C. Bauer, A. Stadler, M. Lindner, M. Jakobi, W. Volk, A. W. Koch, and J. Roths, "In-situ high temperature and large strain monitoring during a copper casting process based on regenerated fiber Bragg grating sensors," J. Lightwave Technol. **39**, 6660 (2021).

113. D. Barrera, V. Finazzi, J. Villatoro, S. Sales, and V. Pruneri, "Performance of a high-temperature sensor based on regenerated fiber Bragg gratings," Proc. SPIE **7753**, 775381 (2011).

114. V. R. Mamidi, S. Kamineni, L. N. S. P. Ravinuthala, V. Thumu, and V. R. Pachava, "Characterization of encapsulating materials for fiber Bragg grating-based temperature sensors," Fiber Integr. Opt. **33**, 325 (2014).

115. B. A. Wilson, C. M. Petrie, and T. E. Blue, "High-temperature effects on the light transmission through sapphire optical fiber," J. Am. Ceram. Soc. **101**, 3452 (2018).

116. S. Yang, D. Homa, H. Heyl, L. Theis, J. Beach, B. Dudding, G. Acord, D. Taylor, G. Pickrell, and A. Wang, "Application of Sapphire-Fiber-Bragg-grating-based multi-point temperature sensor in boilers at a commercial power plant," Sensors **19**, 3211 (2019).

117. A. Inoue, "Fabrication and application of fiber Bragg grating: a review," Optoelectron. Dev. Technol. **10**, 119 (1995).

118. S. Gupta, T. Mizunami, T. Yamao, and T. Shimomura, "Fiber Bragg grating cryogenic temperature sensors," Appl. Opt. **35**, 5202 (1996).

119. V. P. Wnuk, A. Méndez, S. Ferguson, and T. Graver, "Process for mounting and packaging of fiber Bragg grating strain sensors for use in harsh environment applications," Proc. SPIE **5758**, 46 (2005).

120. R. H. Selfridge, S. M. Schultz, T. L. Lowder, V. P. Wnuk, A. Méndez, S. Ferguson, and T. Graver, "Packaging of surface relief fiber Bragg gratings for use as strain sensors at high temperature," Proc. SPIE **6167**, 616702 (2006).

121. W. Li, Y.-W. Li, X.-D. Han, and G.-Q. Yu, "The study of enhancing temperature sensitivity for FBG temperature sensor," in *International Conference on Machine Learning and Cybernetics* (2009), p. 2746.

122. M. Fisser, R. A. Badcock, P. D. Teal, S. Janssens, and A. Hunze, "Palladium-based hydrogen sensors using fiber Bragg gratings," J. Lightwave Technol. **36**, 850 (2018).

123. L. Yang, Y. Chen, Z. Xu, H. Xia, T. Natuski, Y. Xi, and Q. Ni, "Effect of surface modification of carbon fiber based on magnetron sputtering technology on tensile properties," Carbon **204**, 377 (2023).

124. S. D. V. S. Jagannadha Raju, S. M. Haque, B. K. Goud, R. De, J. S. Misal, and K. D. Rao, "Fiber Bragg grating sensor for *in situ* substrate temperature measurement in a magnetron sputtering system," Phys. Scr. **97**, 095505 (2022).

125. Z. Li, M. Yang, J. Dai, G. Wang, C. Huang, J. Tang, W. Hu, H. Song, and P. Huang, "Optical fiber hydrogen sensor based on evaporated Pt/WO$_3$ film," Sens. Actuators B **206**, 564 (2015).

126. X. Zhou, Y. Dai, F. Liu, and M. Yang, "Highly sensitive and rapid FBG hydrogen sensor using Pt-WO$_3$ with different morphologies," IEEE Sens. J. **18**, 2652 (2018).

127. D. A. Pinnow, G. D. Robertson, and J. A. Wysocki, "Reductions in static fatigue of silica fibers by hermetic jacketing," Appl. Phys. Lett. **34**, 17 (1979).

128. G. Bubel, J. T. Krause, B. Bickta, and R. Ku, "Mechanical reliability of metallized optical fiber for hermetic terminations," in *Optical Fiber Communication Conference* (1989), paper WA5.

129. J. E. Watson, G. A. Shreve, M. N. Miller, D. Stevens, C. Sykora, D. LaBella, K. Ostby, and W. K. Smith, "Electroless plating of optical fibers for hermetic feedthrough seals," in *50th Electronic Components and Technology Conference* (2000), p. 250.

130. S. Sandlin, T. Kinnunen, J. Rämö, and M. Sillanpää, "A simple method for metal re-coating of optical fibre Bragg gratings," Surf. Coat. Technol. **201**, 3061 (2006).

131. S. Sandlin, T. Kosonen, A. Hokkanen, and L. Heikinheimo, "Use of brazing technique for manufacturing of high temperature fibre optical temperature and displacement transducer," Mater. Sci. Technol. **23**, 1249 (2007).

132. M. S. Müller, L. Hoffmann, T. Lautenschlager, and A. W. Koch, "Soldering fiber Bragg grating sensors for strain measurement," in *19th International Conference on Optical Fibre Sensors* (2008), p. 61.

133. Y.-L. Wang, Y. Tu, and S.-T. Tu, "Development of highly-sensitive and reliable fiber Bragg grating temperature sensors with gradient metallic coatings for cryogenic temperature applications," IEEE Sens. J. **21**, 4652 (2021).

134. J. Liang, Y. Yu, Q. Bian, W. Xu, Z. Wang, S. Zhang, J. Weng, J. Zhu, Y. Chen, X. Hu, J. Yang, and Z. Zhang, "Metal-coated high-temperature strain optical fiber sensor based on cascaded air-bubble FPI-FBG structure," Opt. Express **31**, 16795 (2023).

135. R. O. Claus, C. E. Lee, J. J. Alcoz, W. N. Gibler, R. A. Atkins, H. F. Taylor, and E. Udd, "Method for embedding optical fibers and optical fiber sensors in metal parts and structures," Proc. SPIE **1588**, 110 (1991).

136. G. Lin, L. Wang, C. Yang, M. Shih, and T. Chuang, "Thermal performance of metal-clad fiber Bragg grating sensors," IEEE Photon. Technol. Lett. **10**, 406 (1998).

137. Q. Bian, C. Bauer, A. Stadler, F. Buchfellner, M. Jakobi, W. Volk, A. W. Koch, and J. Roths, "Monitoring strain evolution and distribution during the casting process of AlSi$_9$Cu$_3$ alloy with optical fiber sensors," J. Alloys Compd. **935**, 168146 (2023).

138. Q. Bian, A. Podhrazsky, C. Bauer, A. Stadler, F. Buchfellner, R. Kuttler, M. Jakobi, W. Volk, A. W. Koch, and J. Roths, "Temperature and external strain sensing with metal-embedded optical fiber sensors for structural health monitoring," Opt. Express **30**, 33449 (2022).

139. Y. Guo, L. Xiong, and H. Liu, "Research on the durability of metal-packaged fiber Bragg grating sensors," IEEE Photon. Technol. Lett. **31**, 525 (2019).

140. J. Lei, Q. Zhang, Y. Song, J. Tang, J. Tong, F. Peng, and H. Xiao, "Laser-assisted embedding of all-glass optical fiber sensors into bulk ceramics for high-temperature applications," Opt. Laser Technol. **128**, 106223 (2020).

141. J. Mathew, C. Hauser, P. Stoll, C. Kenel, D. Polyzos, D. Havermann, W. N. MacPherson, D. P. Hand, C. Leinenbach, A. Spierings, K. Koenig-Urban, and R. R. J. Maier, "Integrating fiber Fabry-Perot cavity sensor into 3-D printed metal components for extreme high-temperature monitoring applications," IEEE Sens. J. **17**, 4107 (2017).

142. A. Ghazanfari, W. Li, M. C. Leu, Y. Zhuang, and J. Huang, "Advanced ceramic components with embedded sapphire optical fiber sensors for high temperature applications," Mater. Des. **112**, 197 (2016).

143. Y. Zhang, L. Zhu, F. Luo, M. Dong, R. Yang, W. He, and X. Lou, "Comparison of metal-packaged and adhesive-packaged fiber Bragg grating sensors," IEEE Sens. J. **16**, 5958 (2016).

144. A. Hehr, M. Norfolk, J. Wenning, J. Sheridan, P. Leser, P. Leser, and J. A. Newman, "Integrating fiber optic strain sensors into metal using ultrasonic additive manufacturing," JOM **70**, 315 (2018).

145. C. Mou, P. Saffari, D. Li, K. Zhou, L. Zhang, R. Soar, and I. Bennion, "Smart structure sensors based on embedded fibre Bragg grating arrays in aluminium alloy matrix by ultrasonic consolidation," Meas. Sci. Technol. **20**, 034013 (2009).

146. X. Li, J. Johnson, J. Groza, and F. Prinz, "Processing and microstructures of fiber Bragg grating sensors embedded in stainless steel," Metall. Mater. Trans. A **33**, 3019 (2002).

147. H. Alemohammad and E. Toyserkani, "Metal embedded optical fiber sensors: laser-based layered manufacturing procedures," J. Manuf. Sci. Eng. **133**, 031015 (2011).

148. R. Zou, X. Liang, R. Cao, S. Li, A. To, P. Ohodnicki, M. Buric, and K. Chen, "Optical fiber sensor-fused additive manufacturing and its applications in residual stress measurements," in *CLEO: Applications and Technology* (2017), paper AW1B.2.

149. S. I. Kim, H. Y. Jung, S. Yang, J. Yoon, H. Lee, and W. Ryu, "3D printing of a miniature turbine blade model with an embedded fibre Bragg grating sensor for high-temperature monitoring," Virtual Phys. Prototyp. **17**, 156 (2022).

150. C. Zhang, H. Yu, D. Sun, and W. Liu, "Ultrasonic additive manufacturing of metallic materials," Metals **12**, 1912 (2022).

151. R. Dehoff and S. Babu, "Characterization of interfacial microstructures in 3003 aluminum alloy blocks fabricated by ultrasonic additive manufacturing," Acta Mater. **58**, 4305 (2010).

152. C. Y. Kong, R. C. Soar, and P. M. Dickens, "Ultrasonic consolidation for embedding SMA fibres within aluminium matrices," Compos. Struct. **66**, 421 (2004).

153. Y. Li, W. Liu, Y. Feng, and H. Zhang, "Ultrasonic embedding of nickel-coated fiber Bragg grating in aluminum and associated sensing characteristics," Opt. Fiber Technol. **18**, 7 (2012).

154. Y. Zhang, L. Zhu, F. Luo, M. Dong, X. Ding, and W. He, "Fabrication and characterization of metal-packaged fiber Bragg grating sensor by one-step ultrasonic welding," Opt. Eng. **55**, 067103 (2016).

155. J. J. Schomer and M. J. Dapino, "High temperature characterization of fiber bragg grating sensors embedded into metallic structures through ultrasonic additive manufacturing," in *Proceedings of the ASME 2017 Conference on Smart Materials, Adaptive Structures and Intelligent Systems* (2017), paper V002T05A003.

156. C. M. Petrie, N. Sridharan, M. Subramanian, A. Hehr, M. Norfolk, and J. Sheridan, "Embedded metallized optical fibers for high temperature applications," Smart Mater. Struct. **28**, 055012 (2019).

157. H. C. Hyer, D. C. Sweeney, and C. M. Petrie, "Functional fiber-optic sensors embedded in stainless steel components using ultrasonic additive manufacturing for distributed temperature and strain measurements," Addit. Manuf. **52**, 102681 (2022).

158. M. Xu, J. Archambault, L. Reekie, and J. Dakin, "Discrimination between strain and temperature effects using dual-wavelength fibre grating sensors," Electron. Lett. **30**, 1085 (1994).

159. P. Zhang, H. Yang, Y. Wang, H. Liu, K. S. Lim, D. S. Gunawardena, and H. Ahmad, "Strain measurement at temperatures up to 800°C using regenerated gratings produced in the high Ge-doped and B/Ge co-doped fibers," Appl. Opt. **56**, 6073 (2017).

160. H. Liu, H. Z. Yang, X. Qiao, M. Hu, Z. Feng, R. Wang, Q. Rong, D. S. Gunawardena, K.-S. Lim, and H. Ahmad, "Strain measurement at high temperature environment based on Fabry-Perot interferometer cascaded fiber regeneration grating," Sens. Actuators A **248**, 199 (2016).

161. Y. Wang, H. Bao, Z. Ran, J. Huang, and S. Zhang, "Integrated FP/RFBG sensor with a micro-channel for dual-parameter measurement under high temperature," Appl. Opt. **56**, 4250 (2017).

162. T. Yang, Z. Ran, X. He, Z. Li, Z. Xie, Y. Wang, Y. Rao, X. Qiao, Z. He, P. He, Y. Yang, and F. Min, "Temperature-compensated multifunctional all-fiber sensors for precise strain/high-pressure measurement," J. Lightwave Technol. **37**, 4634 (2019).

163. K. Naeem, Y. Chung, and B. H. Kim, "Cascaded two-core PCFs-based in-line fiber interferometer for simultaneous measurement of strain and temperature," IEEE Sens. J. **19**, 3322 (2019).

164. Q. Yan, W. Liu, S. Duan, C. Sun, S. Zhang, Z. Han, X. Jin, L. Zhao, T. Geng, W. Sun, and L. Yuan, "A cascade structure made by two types of gratings for simultaneous measurement of temperature and strain," Opt. Fiber Technol. **42**, 105 (2018).

165. K. Markowski, K. Jedrzejewski, M. Marzecki, and T. Osuch, "Linearly chirped tapered fiber-Bragg-grating-based Fabry-Perot cavity and its application in simultaneous strain and temperature measurement," Opt. Lett. **42**, 1464 (2017).

166. B. Hopf, F. J. Dutz, T. Bosselmann, M. Willsch, A. W. Koch, and J. Roths, "Iterative matrix algorithm for high precision temperature and force decoupling in multi-parameter FBG sensing," Opt. Express **26**, 12092 (2018).

167. F. Buchfellner, Q. Bian, W. Hu, X. Hu, M. Yang, A. W. Koch, and J. Roths, "Temperature-decoupled hydrogen sensing with Pi-shifted fiber Bragg gratings and a partial palladium coating," Opt. Lett. **48**, 73 (2023).

168. M. Song, S. B. Lee, S. S. Choi, and B. Lee, "Simultaneous measurement of temperature and strain using two fiber Bragg gratings embedded in a glass tube," Opt. Fiber Technol. **3**, 194 (1997).

169. Q. Tian, G. Xin, K.-S. Lim, Y. He, J. Liu, H. Ahmad, X. Liu, and H. Yang, "Cascaded Fabry-Perot interferometer-regenerated fiber Bragg grating structure for temperature-strain measurement under extreme temperature conditions," Opt. Express **28**, 30478 (2020).

170. S. Sarkar, D. Inupakutika, M. Banerjee, M. Tarhani, and M. Shadaram, "Machine learning methods for discriminating strain and temperature effects on FBG-based sensors," IEEE Photon. Technol. Lett. **33**, 876 (2021).

171. K. Dey, N. Vangety, and S. Roy, "Machine learning approach for simultaneous measurement of strain and temperature using FBG sensor," Sens. Actuators A **333**, 113254 (2022).

172. C. Deng, M. Yu, L. Zhu, J. Xia, and M. Dong, "A deep learning algorithm ADPNet for strain and temperature decoupling of fiber Bragg gratings," Opt. Fiber Technol. **79**, 103356 (2023).

173. J. Wang, B. Dong, E. Lally, J. Gong, M. Han, and A. Wang, "Multiplexed high temperature sensing with sapphire fiber air gap-based extrinsic Fabry-Perot interferometers," Opt. Lett. **35**, 619 (2010).

174. C. Du, W. Xie, S. Meng, Y. Yin, L. Jiao, and L. Song, "The connection technology based on high temperature silica fiber optic sensor," Proc. SPIE **8345**, 83452X (2012).

175. P. Dragic, T. Hawkins, P. Foy, S. Morris, and J. Ballato, "Sapphire-derived all-glass optical fibres," Nat. Photonics **6**, 627 (2012).

176. T. Elsmann, A. Lorenz, N. S. Yazd, T. Habisreuther, J. Dellith, A. Schwuchow, J. Bierlich, K. Schuster, M. Rothhardt, L. Kido, and H. Bartelt, "High temperature sensing with fiber Bragg gratings in sapphire-derived all-glass optical fibers," Opt. Express **22**, 26825 (2014).

177. B. A. Wilson and T. E. Blue, "Creation of an internal cladding in sapphire optical fiber using the ^{6}Li(n, α)^{3}H reaction," IEEE Sens. J. **17**, 7433 (2017).

178. Q. Guo, Z. Jia, X. Pan, S. Liu, Z. Tian, Z. Zheng, C. Chen, G. Qin, and Y. Yu, "Sapphire-derived fiber Bragg gratings for high temperature sensing," Crystals **11**, 946 (2021).

179. Q. Guo, S. Liu, X. Pan, B. Wang, Z. Tian, C. Chen, Q. Chen, Y. Yu, and H. Sun, "Femtosecond laser inscribed helical sapphire fiber Bragg gratings," Opt. Lett. **46**, 4836 (2021).

180. M. Wang, P. S. Salter, F. P. Payne, A. Shipley, S. M. Morris, M. J. Booth, and J. A. Fells, "Single-mode sapphire fiber Bragg grating," Opt. Express **30**, 15482 (2022).

181. J. T. Jones, A. Birri, T. E. Blue, D. Kominsky, K. McCary, O. J. Ohanian, and S. D. Rountree, "Light propagation considerations for internally clad sapphire optical fiber using the ^{6}Li(n,α)^{3}H reaction," J. Lightwave Technol. **40**, 1181 (2022).

182. Q. Bian, H. Zhu, J. Liang, Y. Yu, and P. Yan, "High-order modes suppression in sapphire fiber Bragg gratings based on mode field matching fusion splicing for single-mode demodulation systems," IEEE Sens. J. **23**, 16953 (2023).

183. S. Bera, B. Liu, Y. N. Picard, B. Howard, M. Buric, and P. Ohodnicki, "Fabrication and evaluation of sol-gel derived magnesium aluminate spinel-clad sapphire fiber," Opt. Fiber Technol. **68**, 102801 (2022).

184. X. Luan, R. Yu, Q. Zhang, S. Zhang, and L. Cheng, "Boron nitride coating of sapphire optical fiber for high temperature sensing applications," Surf. Coat. Technol. **363**, 203 (2019).

185. J. Wang, E. M. Lally, X. Wang, J. Gong, G. Pickrell, and A. Wang, "ZrO$_2$ thin-film-based sapphire fiber temperature sensor," Appl. Opt. **51**, 2129 (2012).

186. S. Chen, Q. Zhang, X. Luan, R. Yu, Q. Zhang, S. Zhang, and L. Cheng, "Sapphire optical fiber with SiBCN coating prepared by chemical vapor deposition for high-temperature sensing applications," Thin Solid Films **709**, 138242 (2020).

187. H. Chen, M. Buric, P. R. Ohodnicki, J. Nakano, B. Liu, and B. T. Chorpening, "Review and perspective: sapphire optical fiber cladding development for harsh environment sensing," Appl. Phys. Rev. **5**, 011102 (2018).

188. Q. Bian, H. Zhu, J. Liang, Y. Yu, and P. Yan, "High-order modes suppression in sapphire fiber Bragg gratings based on mode field matching fusion splicing for single-mode demodulation systems," IEEE Sens. J. **23**, 16953 (2023).